Microbreaking and the enhancement of air-water transfer velocity

C. J. Zappa,[1] W. E. Asher, and A. T. Jessup
Applied Physics Laboratory, University of Washington, Seattle, Washington, USA

J. Klinke
Physical Oceanography Research Division, Scripps Institution of Oceanography, La Jolla, California, USA

S. R. Long
NASA Goddard Space Flight Center/Wallops Flight Facility, Wallops Island, Virginia, USA

Received 9 April 2003; revised 4 June 2004; accepted 15 July 2004; published 27 August 2004.

[1] The role of microscale wave breaking in controlling the air-water transfer of heat and gas is investigated in a laboratory wind-wave tank. The local heat transfer velocity, k_H, is measured using an active infrared technique and the tank-averaged gas transfer velocity, k_G, is measured using conservative mass balances. Simultaneous, colocated infrared and wave slope imagery show that wave-related areas of thermal boundary layer disruption and renewal are the turbulent wakes of microscale breaking waves, or microbreakers. The fractional area coverage of microbreakers, A_B, is found to be 0.1–0.4 in the wind speed range 4.2–9.3 m s^{-1} for cleaned and surfactant-influenced surfaces, and k_H and k_G are correlated with A_B. The correlation of k_H with A_B is independent of fetch and the presence of surfactants, while that for k_G with A_B depends on surfactants. Additionally, A_B is correlated with the mean square wave slope, $\langle S^2 \rangle$, which has shown promise as a correlate for k_G in previous studies. The ratio of k_H measured inside and outside the microbreaker wakes is 3.4, demonstrating that at these wind speeds, up to 75% of the transfer is the direct result of microbreaking. These results provide quantitative evidence that microbreaking is the dominant mechanism contributing to air-water heat and gas transfer at low to moderate wind speeds. *INDEX TERMS:* 4504 Oceanography: Physical: Air/sea interactions (0312); 0312 Atmospheric Composition and Structure: Air/sea constituent fluxes (3339, 4504); 3339 Meteorology and Atmospheric Dynamics: Ocean/atmosphere interactions (0312, 4504); 4506 Oceanography: Physical: Capillary waves; 4568 Oceanography: Physical: Turbulence, diffusion, and mixing processes; *KEYWORDS:* microbreaking, gas transfer, waves

Citation: Zappa, C. J., W. E. Asher, A. T. Jessup, J. Klinke, and S. R. Long (2004), Microbreaking and the enhancement of air-water transfer velocity, *J. Geophys. Res.*, *109*, C08S16, doi:10.1029/2003JC001897.

1. Introduction

[2] Atmosphere-ocean interaction plays a crucial role in the global biogeochemistry, and a better understanding of air-sea exchange mechanisms and ocean mixing is needed to improve model predictions of the spatial variability of global air-sea fluxes. The flux of a weakly soluble, nonreactive gas such as CO_2 is water-phase controlled [*Liss and Slater*, 1974] and, in the absence of bubbles, determined by the product of the gas transfer velocity, k_G, and the thermodynamic driving potential across the aqueous mass boundary layer (MBL) at the air-sea interface. The gas flux is commonly expressed as

$$F = k_G \Delta\mu, \tag{1}$$

where the driving potential is defined as the difference in chemical potential across the MBL, $\Delta\mu$, and in the case of gases is most conveniently expressed in terms of fugacities. The net flux of heat across the air-sea interface can also be described in terms of a heat transfer velocity, k_H, and the seawater temperature difference across the aqueous thermal boundary layer at the ocean surface. Whether one is referring to the net flux of heat or gas, the transfer velocity characterizes the kinetic rate of exchange across the air-sea interface and implicitly contains the dependence of the transfer process on the physicochemical hydrodynamics.

[3] Conceptual models for the net flux of heat and of sparingly soluble nonreactive gases assume that the magnitude of the transfer velocity is controlled by hydrodynamical processes in the near-surface aqueous phase. For example, boundary layer models for air-water gas exchange assume that molecular diffusion through the MBL provides the dominant resistance to gas transfer [*Asher and Wanninkhof*, 1998]. Using this conceptual model, turbulence increases the flux by thinning the boundary layer, and the transfer velocity incorporates the dependence of the flux

[1]Now at Lamont-Doherty Earth Observatory of Columbia University, Palisades, New York, USA.

0148-0227/04/2003JC001897$09.00

on diffusivity and turbulence. Since the wind stress at the ocean surface plays a central role in the generation of turbulence through the atmosphere-ocean transfer of momentum to the waves and currents, considerable effort has gone into determining empirical relations between transfer velocities and wind speed [see *Wanninkhof and McGillis*, 1999].

[4] Microscale wave breaking, or microbreaking [*Banner and Phillips*, 1974], is the breaking of very short wind waves without air entrainment. Laboratory experiments in wind-wave tunnels provide a growing body of evidence that turbulence generated by microscale wave breaking is the dominant mechanism for air-water gas transfer at low to moderate wind speeds. Laboratory measurements indicate that a wave-related mechanism regulates gas transfer because the transfer velocity correlates with the total mean square wave slope, $\langle S^2 \rangle$ [*Jähne et al.*, 1984, 1987]. Wave slope characterizes the stability of water waves [e.g., *Longuet-Higgins and Cleaver*, 1994] and certain limiting values of slope are typically used to detect and define wave breaking [e.g., *Banner*, 1990]. Therefore *Jähne et al.* [1987] have argued that wave slope is representative of the near-surface turbulence produced by microscale wave breaking.

[5] Microbreaking is widespread over the oceans, and *Csanady* [1990] has proposed that the specific manner by which it affects k_G is the thinning of the aqueous mass boundary layer (MBL) by the intense surface divergence generated during the breaking process. Infrared (IR) techniques have been successfully implemented to detect this visually ambiguous process and have been used to quantify these regions of surface renewal of the MBL caused by microbreakers [*Jessup et al.*, 1997]. The IR signature provided qualitative evidence of the turbulent wakes of microbreakers that is consistent with *Csanady*'s [1990] idea for the effect of microbreaking on the MBL.

[6] Recently, a comprehensive study was performed to show that microbreaking is the dominant mechanism governing k_G at low to moderate wind speeds [*Zappa*, 1999]. Simultaneous and colocated IR and wave slope imagery demonstrated that the IR signature of the disruption of the aqueous thermal boundary layer corresponds directly to the wakes of microbreakers [*Zappa et al.*, 2001]. Concurrently, simultaneous particle image velocimetry and IR imagery showed that vortices are generated behind the leading edge of microbreakers and that the vorticity correlated with k_G [*Siddiqui et al.*, 2001]. Furthermore, k_G was shown to be linearly correlated with the fraction of water surface covered by the wakes of microbreaking, A_B, and this correlation was invariant with the presence of surfactants [*Zappa et al.*, 2001]. This correlation is evidence for a causal link between microbreaking and gas transfer.

[7] The correlation of k_G with wave slope has shown results similar to the correlation of k_G with A_B. *Jähne et al.* [1984, 1987] observed a correlation of k_G with $\langle S^2 \rangle$ for both fetch-limited and unlimited fetch cases, and *Frew* [1997] and *Bock et al.* [1999] showed the correlation was independent of surfactant for the unlimited fetch case. We suggest that the reason k_G correlates with wave slope is that microbreaking is the wave-related mechanism controlling gas transfer and contributes to $\langle S^2 \rangle$.

[8] In order to provide definitive proof that microscale wave breaking is the physical process that regulates k_G at low to moderate wind speeds, experiments were performed in the wind-wave flume at the Air-Sea Interaction Research Facility at NASA Goddard Space Flight Center/Wallops Flight Facility (WFF) in October–December 1998. At this facility, it was possible to make fetch-dependent, concurrent, and colocated measurements of the relevant physical processes associated with air-water transfer. Measurements of infrared and wave slope imagery were made during the experiments at WFF to confirm that the skin layer disruptions observed in the infrared were indeed caused by microbreaking. Measurements were made of A_B and of tank-averaged gas transfer using Helium (He) and sulfur hexafluoride (SF_6). Additionally, we investigated whether microbreakers are the dominant mechanism controlling gas transfer by measuring the local transfer velocity inside and outside the wakes of microbreakers using the active controlled flux technique (ACFT). Finally, measurements are presented that examine the link between microbreaking and the correlation of transfer velocity with $\langle S^2 \rangle$.

2. Experiments

2.1. Facility

[9] The wind-wave flume at the Air-Sea Interaction Research Facility at NASA GSFC/WFF is 18.29 m long, 1.22 m high, and 0.91 m wide, the water depth is 0.76 m, and the air headspace is 0.46 m. The tank is equipped with a water heating/circulation system and a 10-cm thick water-wave-absorbing "beach" made of plastic honeycomb. The facility is instrumented to measure wind speed, friction velocity, and surface displacement. In addition, for this study, measurements were made of tank-averaged gas transfer, bulk water temperature, air temperature, relative humidity, and bulk flow velocity.

2.2. Gas Transfer Measurement by a Conservative Mass Balance

[10] The gas flux across the air-water interface, F, is calculated from the change of the mean gas concentration in the tank with time by

$$F = -H\frac{dC}{dt}, \tag{2}$$

where H is the mean depth of the tank and C is the depth-averaged gas concentration. Combining equations (1) and (2) yields

$$k_G = \frac{-H(dC/dt)}{(C_w - LC_a)}, \tag{3}$$

where $\Delta\mu$ is approximately equal to $C_w - LC_a$, C_w is the gas concentration in the water at the base of the MBL, C_a is the gas concentration in the air just above the interface, L is the Ostwald solubility, and LC_a is the gas concentration in water if it is in equilibrium with the gas concentration in the air ($=C_o$). If the water is well mixed with respect to tracer gas concentration, $C_w = C$ and upon integration of equation (3) over Δt

$$k_G = \frac{H}{\Delta t}\ln\frac{(C_i - C_o)}{(C_f - C_o)}, \tag{4}$$

where C_i and C_f are the initial and final mean tracer gas concentrations in the tank, respectively.

[11] Tank-averaged gas transfer velocities were determined by a conservative mass balance for He (Schmidt

Table 1. Environmental Conditions for the Wallops Study[a]

U, m s^{-1}	ΔT, °C	ΔT_{aw}, °C	T_w, °C	RH, %	f_p, Hz	RMS η, cm	Ω, m	Experiment
4.8	0.9	−6.5	31.1	57.9	NA	NA	5.6	1
8.3	0.8	−5.5	31.1	61.9	NA	NA	5.6	2
4.2	0.9	−6.7	31.0	50.5	4.6	0.24	5.6	3
8.1	0.8	−6.2	29.8	44.6	2.9	0.68	5.6	4
6.9	0.7	−5.5	27.8	42.1	3.2	0.53	5.6	5
5.6	0.7	−5.4	28.8	43.8	3.6	0.39	5.6	6
8.3	0.7	−5.1	29.7	45.8	2.9	0.67	5.6	7
5.5	0.6	−5.8	28.5	46.3	3.6	0.40	5.6	8
8.3	0.9	−6.8	29.1	68.6	2.9	0.51	5.6	9[b]
5.6	1.0	−7.4	29.9	64.4	3.7	0.32	5.6	10[b]
9.3	1.0	−7.1	29.4	43.2	2.6	0.79	5.6	11[b]
8.3	1.0	−6.6	27.6	41.8	2.9	0.58	5.6	12[b]
6.9	0.8	−5.6	27.7	47.2	3.2	0.43	5.6	13[b]
7.2	1.0	−7.7	30.9	69.2	2.5	0.80	11.1	14[c]
6.1	0.9	−7.0	30.9	76.0	2.7	0.63	11.1	15[c]
5.1	1.1	−8.3	29.7	40.8	2.9	0.52	11.1	16[c]
4.3	1.1	−8.1	29.5	41.6	3.4	0.37	11.1	17[c]
5.2	0.7	−5.0	27.0	39.0	2.9	0.55	11.1	18
6.3	0.7	−5.6	28.2	51.9	2.6	0.71	11.1	19
7.4	1.0	−8.9	30.5	44.4	2.4	0.91	11.1	20
7.4	1.0	−6.6	27.7	45.2	2.5	0.68	11.1	21[b]

[a]Wind speed (U), bulk skin temperature difference (ΔT), air-water temperature difference (ΔT_{aw}), water temperature (T_w), relative humidity (RH), the peak wave frequency (f_p), and the root mean square (RMS) surface displacement (η) have been averaged for the duration of each experiment. Fetch (Ω) is measured to the top of the infrared image and experiment numbers increase in chronological order and were performed over a 1-month time period. The large air-water temperature differences were used to ensure a measurable infrared signal and did not affect the determination of k. NA denotes data that are not available.

[b]Experiments with the surfactant Triton X-100.

[c]Experiments with Terostat.

number, Sc = 94 at 31.5°C; $Sc = \nu/D$, where ν is the kinematic viscosity of water and D is the gas diffusivity in water) and SF_6 (Sc = 510 at 31.5°C) by supersaturating the water with the gases and measuring the decrease in their concentration over time [*Asher et al.*, 1996]. Gas concentrations were measured by gas chromatography using a Carle model 1100 thermal conductivity detector (Chandler Engineering Company, Tulsa, Oklahoma) for He and a Hewlett Packard model 5790 electron capture detector (Hewlett Packard Company, Palo Alto, California) for SF_6. Both chromatographic measurements of gas concentration had an accuracy of ±4%. The concentration measurements made as a function of fetch and depth verified that the tank was well mixed with respect to the timescales of gas transfer. At each sampling time, a tank-averaged concentration, $C(t)$, was calculated from the individual concentrations at the five sampling locations. Following from equation (4), an average k_G was calculated as the slope of the line given by plotting $-H \ln [C(t)/C_i]$ versus time since the air tracer gas concentration was negligible (i.e., C_o = 0). Three samples were drawn at evenly spaced depths at the test section located at 5.5 m as well as a middepth sample 4.0 m upstream and a middepth sample 3.5 m downstream of the test section.

[12] The environmental conditions were continuously monitored throughout the experiment. Table 1 summarizes the conditions during the 21 experiments conducted for the Wallops study. The duration of each experiment was determined by the gas transfer measurement of He and SF_6 by conservative mass balance and lasted between 1.5 and 3.5 hours. The Schmidt number exponent, n, was calculated by

$$n = \frac{\ln[k_1/k_2]}{\ln[Sc_2/Sc_1]}, \tag{5}$$

where the subscripts 1 and 2 correspond to He and SF_6, respectively.

2.3. Fetch, Surfactants, and Waves

[13] To investigate the dependence of gas transfer and microscale wave breaking on fetch, measurements were made at two fetches of 5.6 m and 11.1 m. Figure 1 shows the experimental setup used at both fetches. The water used in the tank was filtered tap water, and the surface was skimmed before each experiment to remove accumulated surface contaminants. Biological activity was minimized by continuous bromination to 5 ppm levels using dissolving pellets of 1-bromo-3-chloro-5,5-dimethylhydantoin (Bio-Lab Inc., Decatur, Georgia). As a further precaution, the tank was drained, cleaned, and refilled between the groups of experiments performed at the two fetches.

[14] The influence of surfactants also was investigated by purposely adding 1 g m^{-3} of the soluble surfactant Triton X-100 (polyoxyethyleneisooctylphenyl ether, Aldrich Chemical Co., Milwaukee, Wisconsin) to the water for a portion of the experiments at both fetches. During four experiments at the 11.1 m fetch, a putty, Terostat MS939 (Sahlberg, Feldkirchen bei München, Germany), was used to reseal the light box used for the image slope system and slowly bled a surface-active contaminant into the water. The water for these experiments immediately following the change in fetch (experiments 14–17) was not treated with Triton X-100, but the presence of this contaminant made these experiments effectively surfactant-influenced cases. After observing lower transfer velocities and a Schmidt number exponent of $^2/_3$, characteristic of surfactant contamination, the tank was drained, the Terostat was removed, and the tank was cleaned and refilled. Subsequent measurements of the gas transfer velocities and Schmidt number exponent showed no further evidence of surface contami-

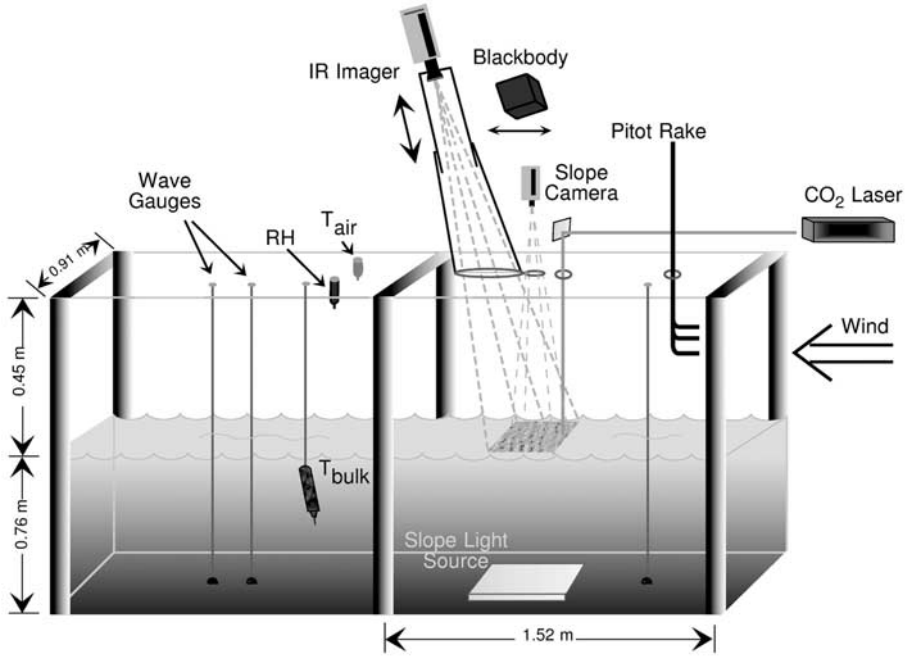

Figure 1. Experimental setup for a given fetch during the Wallops study.

nation. The surface conditions for experiments 14 through 17 therefore have been denoted as Terostat cases.

[15] Spectra for the wire wave gauge measurements of the surface displacement are shown in Figure 2 for a variety of fetch, wind speed, and surfactant conditions. The spectra have been averaged over the duration of each experiment, and truncated at 30 Hz because of the response of the wire wave gauges. All spectra show a distinct narrow banded peak, associated higher harmonics, and a falloff above 10 Hz that approaches a slope of −3.5. For spectra at the 5.6 m fetch, wave energy increases with wind speed and wave frequency decreases. The spectra at the 11.1 m fetch, even at a lower wind speed, show increased energy and a decreased peak frequency compared to the shorter fetch. Experiments performed with Triton X-100 show a distinct decrease in energy and a slight increase in frequency from cleaned cases at the same wind speed and fetch. The peak wave frequency and root mean square surface displacement are summarized for the study in Table 1.

2.4. Infrared and Wave Slope Imagery

[16] Infrared imagery was used to detect and quantify the fractional coverage of microscale wave breaking, A_B, and to implement the ACFT. Two simultaneous sequences of infrared and wave slope imagery were taken at three equal intervals during the course of the experiment, for a total of six runs for each pair of techniques. The infrared measurements were made using an Amber model Radiance HS infrared imager (Amber Engineering, Goleta, CA) that responds to radiation in the spectral band of 3–5 μm. At a range of 1.4 m and an incidence angle of 30°, the imager viewed a surface area with a vertical scale of 52 cm and a horizontal scale of 51 cm at the top of the image and 47 cm at the bottom. A nonuniformity correction and a calibration were performed before each run during the experiment using a Santa Barbara Infrared model 2004S blackbody (SBIR, Santa Barbara, California). Care was taken throughout the calibration and measurements to minimize reflection effects by using custom fabricated shrouds. Laboratory tests of the imager show a noise-equivalent temperature difference of less than 0.025°C. The infrared imager is ideally suited to measure the skin temperature because the optical depth of the detected infrared radiation, on average 35 μm for the spectral wavelength band of 3–5 μm [*McAlister and McLeish*, 1970; *Downing and Williams*, 1975], is much less than the thickness of the aqueous thermal boundary layer, of $O(10^{-2}–10^{-3})$ m [*McAlister and McLeish*, 1969; *Wu*, 1971; *Hill*, 1972].

[17] Wave slope imagery was used to complement the infrared detection of microbreaking and observe the surface roughness characteristics of the breaking process as they relate to the mean square wave slope. The wave slope imaging system was based on the refractive light techniques developed by *Keller and Gotwols* [1983] and modernized by *Jähne et al.* [1994]. The image slope system is the combination of a Sony XC-75 CCD camera at a range of 3 m to the water surface and a subsurface light box covered by an intensity absorption screen with a linear gradient in the along-tank direction. At this distance of 3 m from the water surface, a wave slope image area of 18 cm by 24 cm was achieved with a wave number resolution of greater than 1000 rad m^{-1}. Areas of bright intensity denote steep leeward (front face of a wave) slope and areas of dark intensity denote steep windward (back face of a wave) slope. The result is a spatial map of a direct measure of the surface slope in the upwind/downwind direction that is proportional to the image intensity. The wave slope imaging system is calibrated to measure upwind/downwind slope from −1.25 to +1.25, and any larger slope was set to the corresponding maximum slope. [*Klinke and Jähne*, 1995;

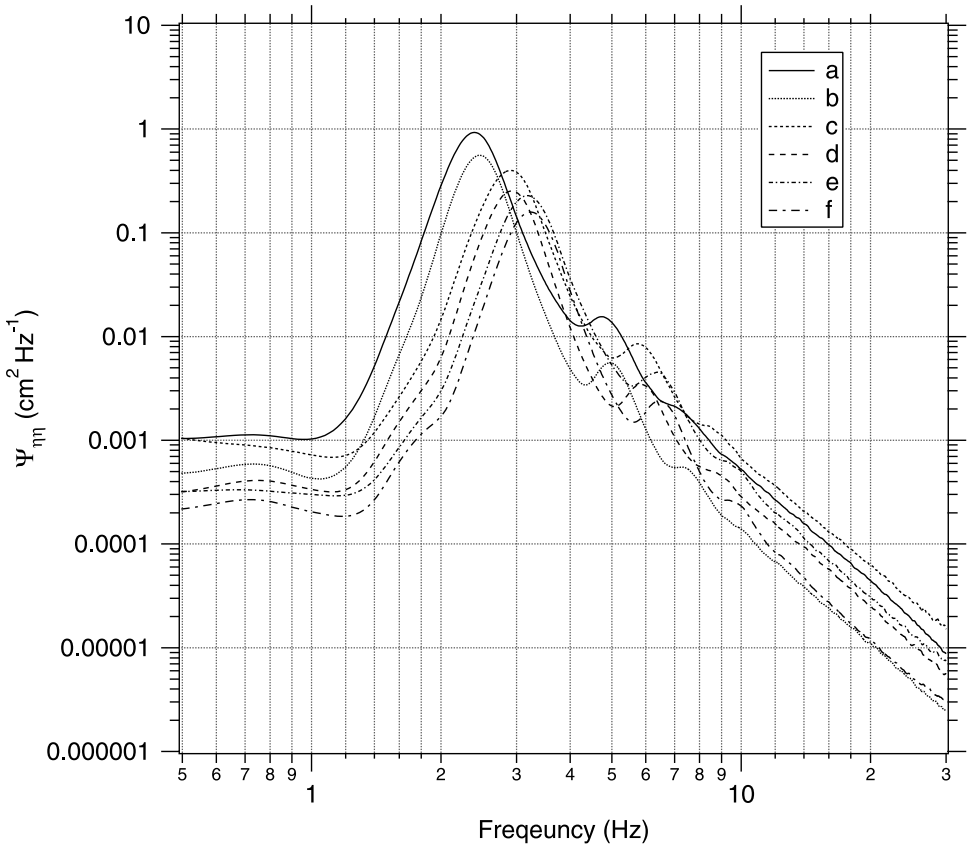

Figure 2. Spectra of surface displacement, $\Psi_{\eta\eta}$, from the wire wave gauge measurements for a variety of fetch (Ω), wind speed (U), and surfactant conditions: (a) Ω = 11.1 m, U = 7.4 m s^{-1}, cleaned; (b) Ω = 11.1 m, U = 7.4 m s^{-1}, Triton X-100; (c) Ω = 5.6 m, U = 8.3 m s^{-1}, cleaned; (d) Ω = 5.6 m, U = 8.3 m s^{-1}, Triton X-100; (e) Ω = 5.6 m, U = 6.9 m s^{-1}, cleaned; and (f) Ω = 5.6 m, U = 6.9 m s^{-1}, Triton X-100.

Klinke, 1996]. The slope images give a direct measure of the mean squared slope, $\langle S^2 \rangle$, by squaring the value for slope at each pixel and taking the mean of this quantity for the whole image.

[18] The fraction of water surface covered by the wakes of microbreaking waves, A_B, was computed by applying a thresholding technique to the infrared images coupled with standard morphological processing operations as outlined by *Zappa* [1999] and *Zappa et al.* [2001]. The threshold is based upon the mean skin temperature specified by the minimum temperature, $\langle T_{\min} \rangle$, within each image and a measure of the bulk skin temperature difference, δT, specified by the standard deviation of the image temperature, σ_T. The threshold of $\langle T_{\min} \rangle + 3.5\sigma_T$ was chosen from a full range of thresholds to detect the features processed as A_B. For the runs used to detect A_B, 1536 frames of infrared imagery were acquired at a frequency of 15 Hz for a record of 100 s in duration. Microscale breaking events are characterized by a front of sharp temperature contrast that propagates with the steep forward face of the wave crest in the slope image, as well as the warm region left behind the propagating front corresponding to the dimpled decaying turbulent wake. The chosen threshold level has been verified using the wave slope imagery and detects microbreaking most reliably for all wind speeds and surface conditions. The comparison of the detected A_B with the slope imagery provides independent verification to substantiate the choice of threshold, and has been incorporated into the microbreaking detection algorithm.

2.5. Active Controlled Flux Technique

[19] The active controlled flux technique (ACFT) [*Haußecker et al.*, 1995; *Zappa*, 1999; *Asher et al.*, 2004; *Atmane et al.*, 2004] uses heat as a proxy tracer for gas to obtain the remote measurement of the local water-side transfer velocity with high spatial resolution and short response times. With the ACFT, the water surface is heated with a CO_2 laser to produce a spot with a measurable temperature difference that can be tracked within a sequence of infrared images. A Synrad model G48-2-28(W) continuous wave 25-W CO_2 laser (Synrad Inc., Mulkilteo, Washington) operating at 10.6 μm was directed at the water surface from above the tank using a series of mirrors and was pulsed for 40 ms with a gating frequency of roughly 1 Hz. The laser beam generated heated patches on the water surface that were roughly 2–3 cm in diameter in the field of view of the infrared imager. The patch was tracked using a Center of Mass (CM) algorithm [*Zappa*, 1999; *Atmane et al.*, 2004]. This CM algorithm detected the warm patch using a threshold temperature of three standard deviations above the mean temperature in the image [*Zappa*, 1999]. The decay curves determined using the CM algorithm were shown to differ by less than 5% from the 3D Structure Tensor tracking algorithm developed by *Haußecker and Jähne* [1997]. For the runs used

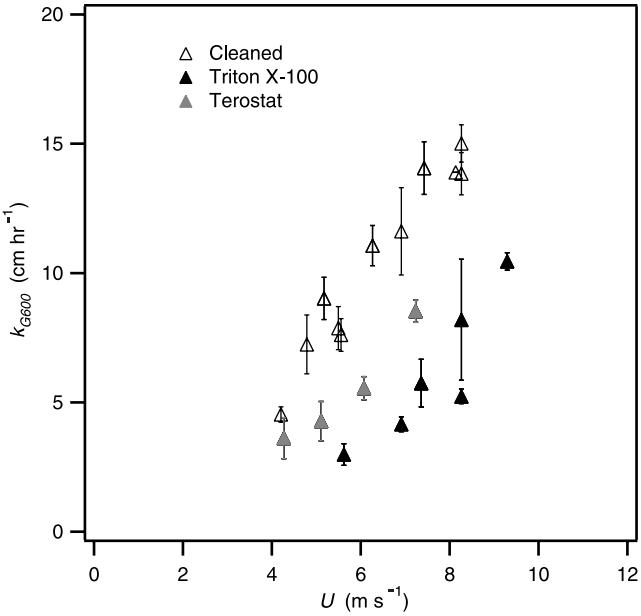

Figure 3. Tank-averaged gas transfer velocity, k_{G600}, for He referenced to a $Sc = 600$ as a function of wind speed, U. The legend specifies the respective surface condition as discussed in section 2.3.

to determine the decay time from the ACFT, the infrared imagery was digitized at a frequency of 120 Hz. A total of 150–180 individual patches were analyzed within an experiment.

[20] The transfer velocity of heat, k_H, is determined from the surface renewal rate, λ, which is estimated from the thermal decay of the heated spot as predicted from a surface renewal model. The method employed by *Haußecker et al.* [1995] fits the normalized surface temperature, T_N, of the patches tracked by the ACFT to

$$T_N = \frac{h}{\sqrt{h^2 + 4\alpha t}} e^{-\lambda t} \tag{6}$$

where h is the penetration depth and α is the thermal diffusivity of water. The analytical solution of the one-dimensional unsteady diffusion equation in equation (6) models turbulent transport characterized by a statistical renewal of the surface layer by large eddies as a chemical reaction term. In this technique, the transfer is assumed to be controlled by water-side processes and the heat flux across the air-water interface into the air is assumed to be minimal [*Jähne et al.*, 1989]. The heat transfer velocity is calculated directly from λ using

$$k_H = \sqrt{\alpha\lambda} \tag{7}$$

where the functional form of equation (7) is specific to a surface renewal model where the probability distribution of the surface element lifetimes is defined by an exponential distribution [*Danckwerts*, 1951]. *Jähne et al.* [1987, 1989] have asserted that the gas transfer velocity, k_G, should scale directly to the transfer velocity of heat by

$$k_G = k_H \left(\frac{Sc}{Pr}\right)^{-n} = k_H (Le)^{-n} \tag{8}$$

where Sc is the Schmidt number of a gas, Pr is the Prandtl number of heat, and Le is the Lewis number. The Schmidt number exponent, n, varies between $^1/_2$ (clean surface) and $^2/_3$ (highly contaminated surface or rigid wall) [*Ledwell*, 1984; *Jähne et al.*, 1987]. According to the scaling predicted by equation (3), previous ACFT laboratory measurements yield values of k_H that, when scaled to a common value of Sc, agree with k_G measured using conventional gaseous tracers [*Jähne et al.*, 1989; *Haußecker et al.*, 1995]. Since the area of the short duration laser-heated patch is of $O(10^{-4})$ m^2 while the effective area for the tracer gas exchange is of $O(10)$ m^2, the influence on k_G of the local change in solubility, and hence gas flux, associated with the nearly 1°C temperature change due to the laser heating of the aqueous mass boundary layer is insignificant compared to the existing supersaturation levels of the tracer addition.

3. Results

3.1. Gas Transfer Velocity and Microbreaking

[21] Figure 3 shows the gas transfer velocity referenced to a $Sc = 600$, k_{G600}, as a function of wind speed, U, for both fetches. Here, the gas transfer velocity is referenced to $Sc = 600$ using

$$k_{G600} = k_G \left(\frac{600}{Sc}\right)^{-n}, \tag{9}$$

where n is calculated for each experiment using both the He and SF_6 data as outlined in section 2.2. Consistent with previous results in wind-wave flumes [*Frew*, 1997; *Zappa et al.*, 2001], k_{G600} was lower at a given U for the Triton X-100 surfactant-influenced experiments. Experiments performed with Tersostat contamination also showed a decrease in k_{G600}. Since k_{G600} is tank-averaged, no fetch dependence of this quantity was observed. The variation in k_{G600} at a given wind speed is the consequence of a variation in the degree of surface contamination. Figure 3 demonstrates the difficulty of using wind speed to parameterize gas transfer since k_{G600} can be a multivalued function of U, depending on the surface cleanliness.

[22] Using simultaneous and colocated measurements of infrared and wave slope imagery, *Zappa et al.* [2001] provided evidence that propagating disruptions observed in infrared imagery of wind-driven water surfaces are produced by steep wind waves with bore-like crests. Figure 4 shows a similar comparison during experiment 5 (U = 6.9 m s^{-1}; cleaned surface) and illustrates that capillary-gravity wave packets evolve into microbreaking waves that disrupt the aqueous thermal boundary layer. The characteristic signature of a microbreaking wave in the infrared imagery consists of an abrupt front of increased temperature that propagates through the image in the direction of the wind at roughly the phase speed of the dominant wave. This distinct propagating front disrupts the surface, leaving behind a decaying turbulent wake of warmer water. As the wake turbulence decays, the skin layer recovers back to its original state as a function of the heat flux and the initial background turbulence [*Zappa et al.*, 1998]. Therefore the scallop-shaped wakes left behind by microbreaking waves vary in size and intensity. Smaller-

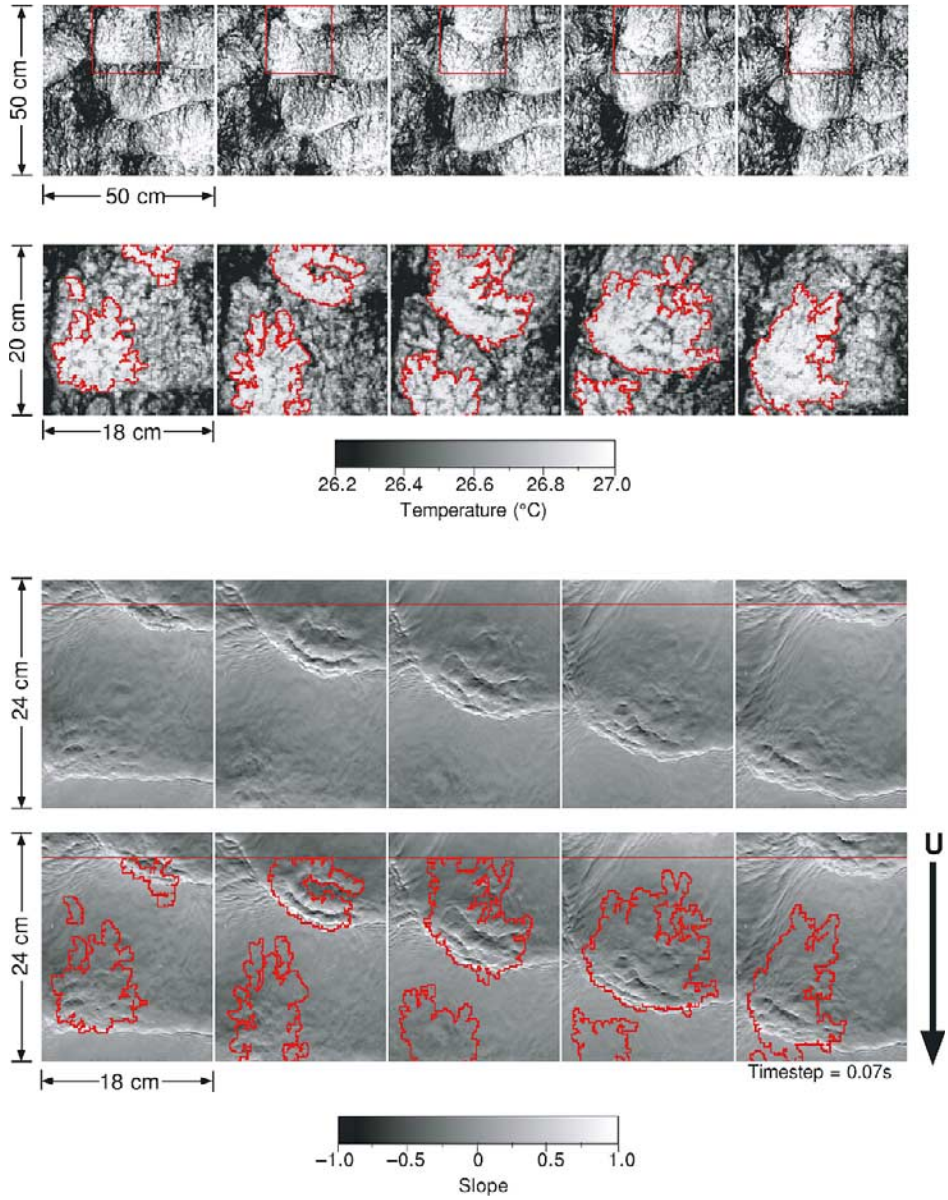

Figure 4. An example of both (top) infrared and (bottom) wave slope imagery at a wind speed of 6.9 m s^{-1} with a cleaned water surface depicting a microscale breaking wave; T_w = 27.2°C, δT_{aw} = −5.6°C, RH = 41.9%, f_p = 3.20 Hz, and Ω = 5.6 m. The disruption of the skin layer imaged in the infrared is coincident with the appearance of a "dimpled" feature on the bore-like crest in the slope imagery. Time increases from left to right in 0.07 s increments, and the wind direction in the images is from top to bottom. The first sequence of infrared images shows a box drawn to highlight the overlapping slope image area. The second infrared sequence is an expanded view of this highlighted region with an outline of the measured A_B. Likewise, only the portion below the line drawn in the slope images corresponds directly to the box (highlighted region) in the infrared images. The second wave slope sequence shows an overlay of the outline of A_B.

scale structures observed in the imagery are most likely associated with background eddies generated by shear, buoyancy (due to the net upward heat flux), and/or turbulence input to the near surface by microbreaking waves. The mixing that produces the infrared signature is the direct consequence of the near-surface turbulence generated by the bore-like crest of the microscale breaking wave.

[23] The outlined features overlaid in the IR and slope imagery shown in Figure 4 contribute to A_B, the ratio of the area of the outlined regions to the total area of the infrared image. Figure 5 shows A_B as a function of wind speed for both fetches. For the cleaned surface cases, A_B increased from 0.25 to 0.40 as the wind speed increased from 4.2 to 8.3 m s^{-1}. With the addition of the surfactant Triton X-100 and for the Terostat cases observed at the 11.1 m fetch, A_B was significantly lower (nearly half) at a given wind speed, consistent with the known ability of surfactants to damp capillary-gravity waves. These measurements of A_B are the

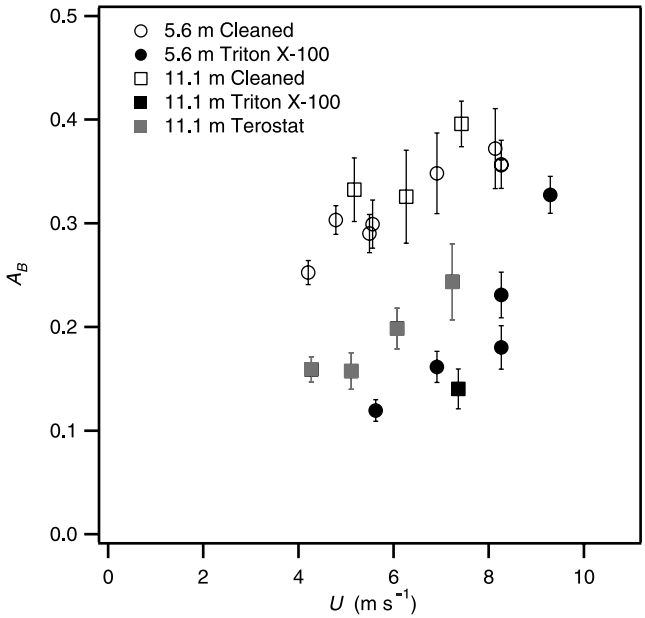

Figure 5. Fractional area coverage of microscale wave breaking, A_B, as a function of wind speed, U. The legend specifies the respective surface condition and fetch as discussed in section 2.3.

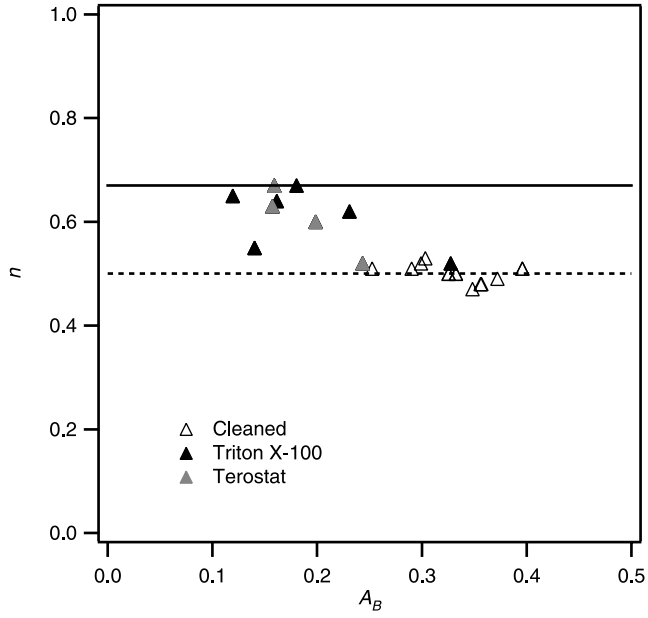

Figure 7. Schmidt number exponent, n, as a function of the fractional area coverage of microscale wave breaking, A_B. See Figure 3 caption for description of legend.

first to cover a wide range of conditions at two fetches, and the values determined here are comparable to previous estimates [*Csanady*, 1990] and measurements [*Jessup et al.*, 1997; *Zappa et al.*, 2001].

[24] Figure 6 shows k_{G600} versus A_B. The data appear to fall into two groups, distinguished as the cleaned and as the surfactant-influenced surfaces, and each is linearly correlated. The coefficient of determination is 0.93 for the cleaned case and 0.94 for the surfactant-influenced case. The linear regression for the cleaned case does not pass through the origin, while that for the surfactant-influenced data nearly does. While conclusive evidence is beyond the scope of this study, the observation of two groupings with respect to surface condition suggests that the complicated dependence of k_{G600} on fetch [*Jähne et al.*, 1989] is further affected by surface contamination [*Lucassen*, 1982; *Frew*, 1997]. Though these coupled effects undoubtedly play a role yet are difficult to discern here, the two distinct groupings are likely the artifact of comparing the tank-averaged k_{G600} with the locally measured A_B. In order to correlate with the k_{G600} measurement, A_B would need to be averaged from measurements at every location down the tank during a given experiment. Rather than make measurements of A_B at all fetches, the active controlled flux technique was used to measure k_H at the same fetch as A_B. The implication is that, in a wind tunnel, it is crucial to compare measurements locally since the processes affecting transfer may vary significantly with fetch.

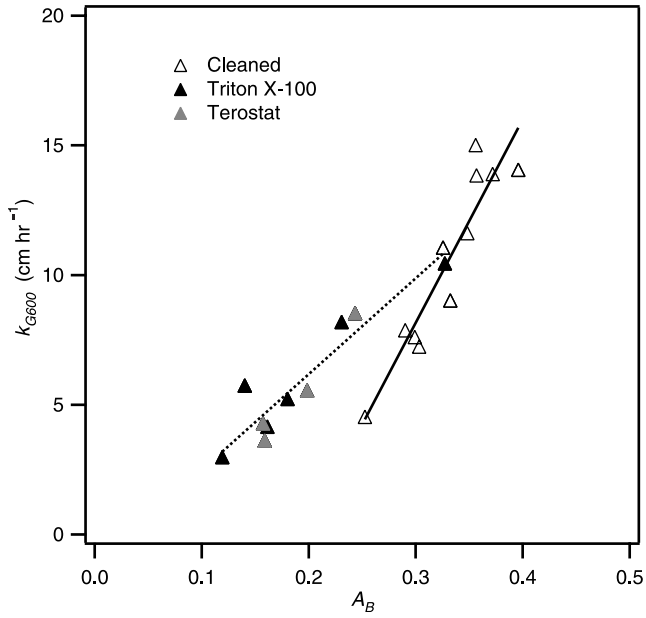

Figure 6. Tank-averaged gas transfer velocity, k_{G600}, for He referenced to a Sc = 600 versus the fractional area coverage of microscale wave breaking, A_B. See Figure 3 caption for description of legend.

[25] The plot of the Schmidt number exponent, n, versus A_B in Figure 7 shows that n decreases from $^2/_3$ to $^1/_2$ as A_B increases from 0.10 to 0.40. The cleaned surface treatments are closely grouped about $^1/_2$ and independent of A_B, while the surfactant-influenced conditions show variability between $^2/_3$ and $^1/_2$. Figure 7 shows that a surfactant-influenced surface does not necessarily result in an n of $^2/_3$.

3.2. Measurements of the Transfer Velocity Using the Active Controlled Flux Technique

[26] The mean normalized surface temperature, T_N, of the patches tracked by the ACFT is shown in Figure 8 as a function of wind speed ranging from 4.2 m s^{-1} to 8.3 m s^{-1}. Assuming the surface cleanliness is constant, the transfer should increase as the wind speed increases. As the wind speed increased, T_N decayed more quickly, and λ increased with wind speed from 2.0 to 7.6 s^{-1}. Since from equation (7) it is seen that k_H increases with λ, Figure 8 implies that k_H

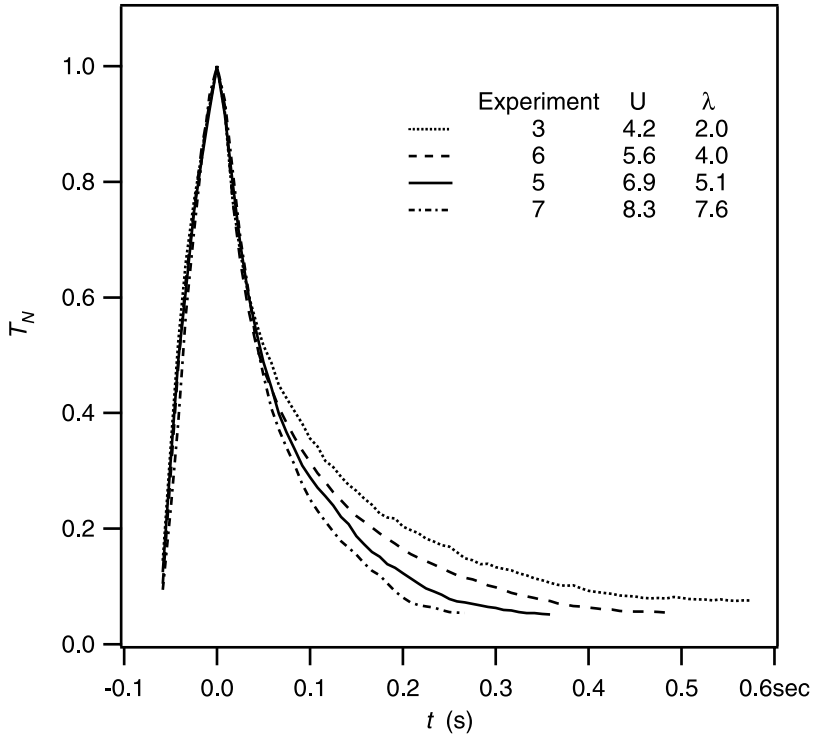

Figure 8. Time series of the normalized surface temperature, T_N, of the tracked ACFT patch varying as a function of wind speed (m s^{-1}) and λ (s^{-1}).

increased with increasing wind speed for the cleaned surface experiments.

[27] According to equation (8), k_G determined by mass balance methods using He and SF_6 should equal k_H determined by the ACFT when scaled by Le^{-n}. Alternatively, replacing k_G with k_H and Sc with Pr, equation (9) can be used to scale k_H to Sc = 600, k_{H600}, in which case k_{G600} should equal k_{H600}. Figure 9 compares k_{H600} and k_{G600} and shows that for this experiment k_{H600} overestimates k_{G600} by a factor of roughly 2.5. This scale factor was determined by minimizing the root mean square error for the difference between the gas and heat transfer velocities. Although a significant difference between k_{H600} and k_{G600} has not been observed in previous comparisons of ACFT-derived k_{H600} values with k_{G600} values measured using bulk gaseous tracers [*Jähne et al.*, 1987, 1989; *Haußecker et al.*, 1995], more recent results from both field and laboratory studies have confirmed that in general when scaled to a common Schmidt number, k_{H600} values do not agree with k_{G600} values [*Richardson*, 2000; *Asher et al.*, 2004; *Atmane et al.*, 2004]. The difference between k_{H600} and k_{G600} observed here cannot be explained by the choice of n, since n was determined independently using He and SF_6 and the values of n are consistent with previous wind tunnel results [*Jähne and Haußecker*, 1998]. Additionally, the discrepancy is too large to be explained by a fetch dependence of k_H. The measurements of k_{H600} at fetches of 5.6 m and 11.1 m both show values at least double those of the tank-averaged k_{G600}. For the tank average of k_{H600} to be equal to k_{G600}, k_{H600} would have to be less than k_{G600} for half of the tank length and greater than k_{G600} for the other half, assuming that k_{H600} increases linearly with fetch. However, the two measurement locations span a distance that represents over 70% of the total tank length, and it is unlikely that k_{H600} over the remaining 30% of the tank area would be small enough to compensate for the majority of the tank area where k_{H600} was over double k_{G600}.

[28] The wind tunnel experiments by *Richardson* [2000] and *Atmane et al.* [2004] and field measurements using ACFT reported by *Asher et al.* [2004] all confirm the presence of a scale factor between k_{H600} and k_{G600} with

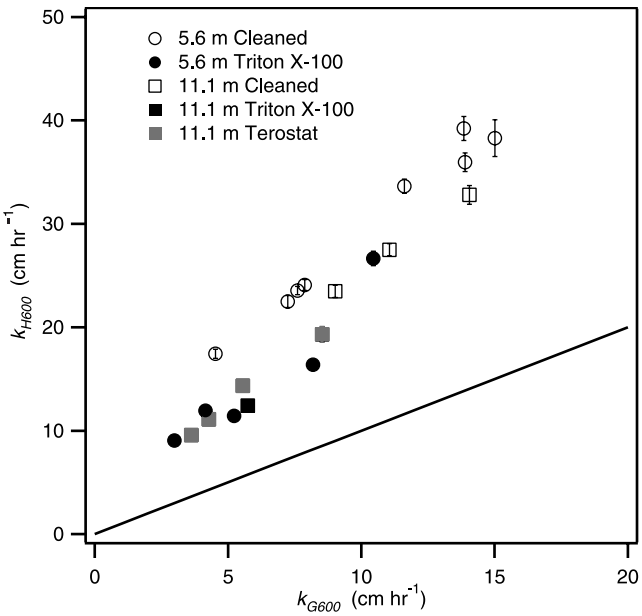

Figure 9. Direct comparison of k_{H600} to k_{G600}. See Figure 5 caption for description of legend.

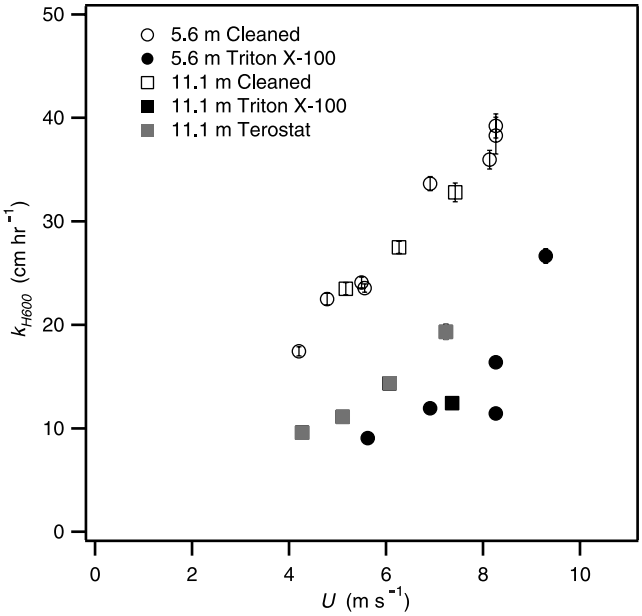

Figure 10. Local heat transfer velocity, k_{H600}, for ACFT referenced to a $Sc = 600$ as a function of wind speed, U. See Figure 5 caption for description of legend.

k_{H600} typically a factor of 2–3 larger than k_{G600}. *Atmane et al.* [2004] proposed modeling the air-water exchange process in terms of surface penetration theory [*Harriott*, 1962] rather than surface renewal. *Atmane et al.* [2004] then showed that because of the difference in diffusive length scales of heat and gas in water, when eddies do not completely renew the water surface and have a nonzero approach distance, surface penetration models predict a scale factor between k_{H600} and k_{G600} that agrees with the scale factors found here and in the other two studies. Although the existence of a scale factor between k_{H600} and k_{G600} is a significant problem in terms of using ACFT to measure gas transfer rates, the scale factor does not affect the use of ACFT for the comparison of local transfer measurements inside and outside of the wakes of microscale breaking waves. The results of *Richardson* [2000], *Atmane et al.* [2004], and *Asher et al.* [2004] suggest that although using ACFT to infer k_{G600} is problematic, the method does provide consistent estimates of k_{H600} for a range of conditions. Here, k_{H600} will refer to the transfer velocity determined by ACFT referenced to $Sc = 600$. However, these k_{H600} values should not be directly compared to historical values of k_{G600}.

[29] Figure 10 shows k_{H600} as a function of wind speed, U, for both fetches. Consistent with the k_{G600} results in Figure 3, k_{H600} was lower at a given U for the Triton X-100 surfactant-influenced experiments. Experiments performed with the Terostat contamination also showed a decrease in k_{H600}. Figure 11 shows that k_{H600} is correlated with A_B, and this correlation is independent of surfactant contamination. A least squares linear regression of all the data gives a coefficient of determination of 0.94, with a slope and y intercept of 106.5 and −6.2, respectively.

3.3. Enhanced Transfer Due to Microbreaking

[30] The correlation between k_{H600} and A_B observed in section 3.2 suggests that microbreaking is the underlying mechanism controlling the gas transfer velocity. If microbreaking is the source of near-surface turbulence responsible for the correlation, the transfer velocity inside the wakes of microbreakers should be enhanced compared to the background. While implementing the ACFT, the individual decay rates of the actively heated patches were observed to vary substantially, and these decay rates were dependent on the influence of microscale wave breaking. *Zappa et al.* [2001] proposed a simple expression for the partitioning of the contribution to the transfer velocity from the areas inside and outside of the wakes as

$$k_H = A_B k_B + (1 - A_B) k_{NB} \tag{10}$$

where k_B is the transfer velocity within A_B and k_{NB} is the transfer velocity outside of A_B. If the expression is valid and $k_B \gg k_{NB}$, we can conclude that microbreaking contributes significantly to the gas transfer velocity. Thus, on the basis of the expression in equation (10), k_H has been partitioned into two separate transfer velocities, one within the wakes of microbreakers disrupting the MBL and one outside the wakes in the background.

[31] An objective of implementing the ACFT is to quantify k_B and k_{NB} to determine the effect that microscale breaking has on the overall k_H. However, the patch decay will depend on the stage of breaking that affects the patch. Figure 12 shows infrared sequences illustrating the three types of decay of the actively heated ACFT patches that have been designated background, delayed microbreaker, and microbreaker. Since not all waves that propagate past a particular point in the image are breaking, "background" ACFT patches are patches that occur in locations that are

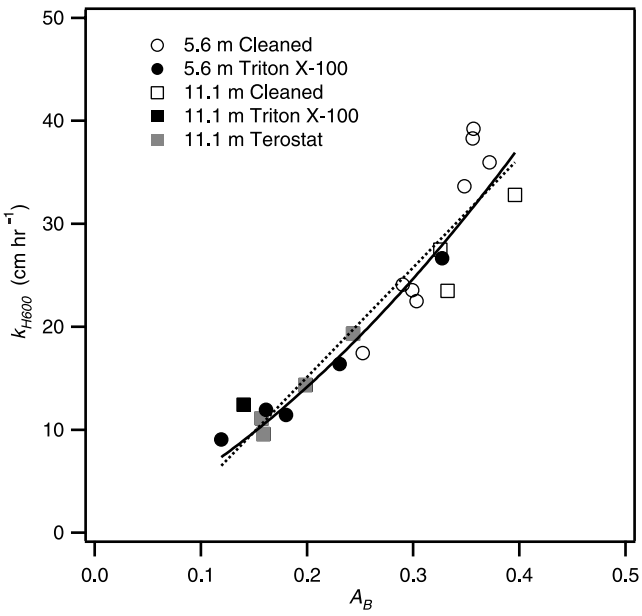

Figure 11. Local transfer velocity, k_{H600}, versus A_B. The dashed line represents a least squares linear regression of k_{H600} against A_B, and the solid line is the partitioning model in equation (10) using the relationship between k_{B600} and A_B in Figure 14 and the mean enhancement factor of 3.4. See Figure 5 caption for description of legend.

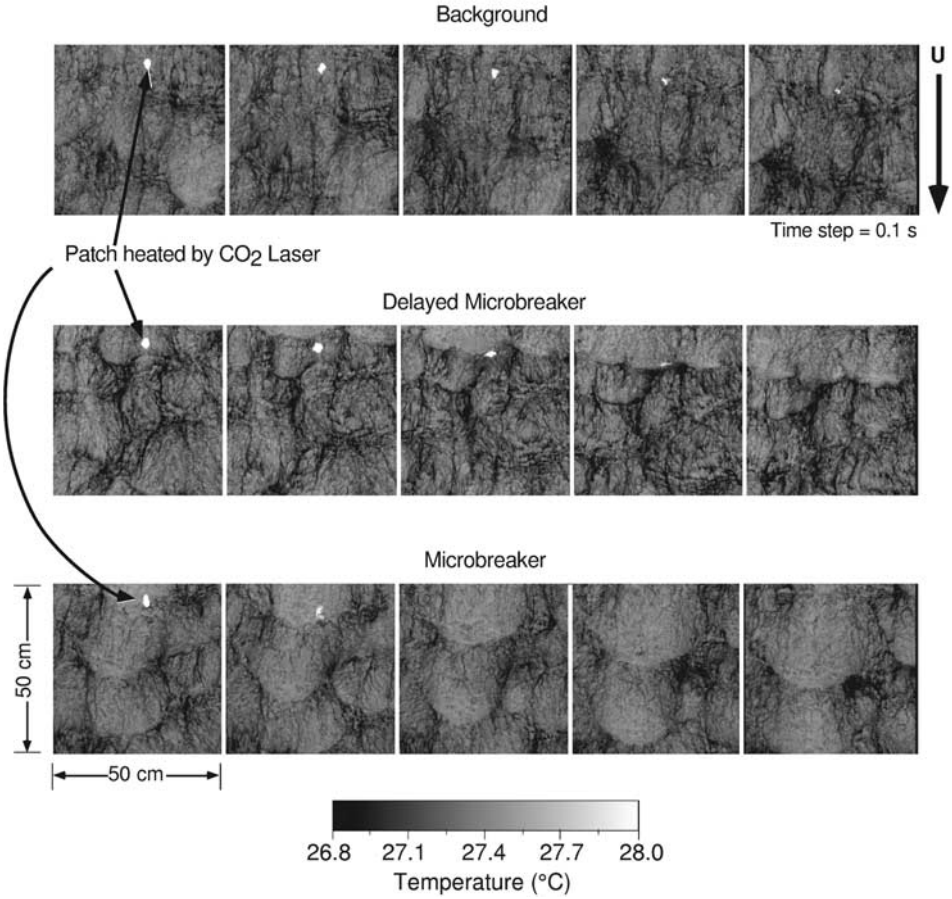

Figure 12. Comparison of ACFT patch decay affected directly by a microscale breaking wave (microbreaker), one that was partially affected by a microscale breaking wave (delayed microbreaker), and one that was not affected at all (background). The experiment number was 5, and the wind speed was 6.9 m s^{-1}. The experimental conditions are identical to those in Figure 4.

unaffected by a microscale breaking wave over the patch lifetime. The top sequence shows a background decay curve, in which the patch is unaffected by microscale breaking and decays slowly. The middle sequence shows the Delayed decay when a patch may decay in the background for a period of time before a microbreaker propagates over the patch and mixes it into the bulk. The decay times for these events vary significantly since the microscale breaking wave may affect it at any time. The bottom sequence shows Microbreaking decay, when a patch is laid directly in the actively breaking wave crest or wake immediately behind the crest of a microscale breaker and decays abruptly as it is mixed completely into the bulk. As shown in these sequences, the patches directly affected by microscale wave breaking decay faster than those patches in the background. These observations are quantified by the normalized decay curve time series, T_N, shown in Figure 13. The comparison of the microbreaker and background sorting will be used to determine the direct effect of microbreaking on k_H.

[32] Distinguishing microbreaker patches from background patches has been achieved by using A_B in the vicinity of the patch. Those patches that were coincident with an active microscale breaking wave were classified as microbreakers and used to determine k_B. Specifically, if at the moment the patch reaches its peak T_N and it is completely within an area of the image designated by A_B, it was classified as a microbreaker. If throughout the whole decay process, the patch is never completely within an area of the image defined by A_B, the patch is classified as background and it was used to compute k_{NB}. Typically, approximately 2 to 12 events from each experiment were determined to be included in k_B and roughly 7 to 12 time series were determined to be included in k_{NB}. The incidence of microbreaker events tended to rise with A_B and the incidence of background events tended to fall with A_B. While A_B provides information on the spatial extent of microbreaking, this observation suggests that the frequency of microscale breaking might be estimated by classifying the ACFT patches directly affected by microscale breaking. However, a statistically significant result would require many more decay time series than available here.

[33] Figure 14 shows k_{B600} and k_{NB600} as a function of A_B, where both k_B and k_{NB} have been referenced to a $Sc = 600$ according to equation (9) using either k_B and k_{NB} in place of k_G and Pr in place of Sc. Both k_{B600} and k_{NB600} increase with A_B, but k_{B600} is significantly greater than k_{NB600}. While it is expected that k_{B600} increases with A_B, it is not surprising that k_{NB600} also varies with A_B, because with the increase in A_B the input of turbulence from microbreakers to the

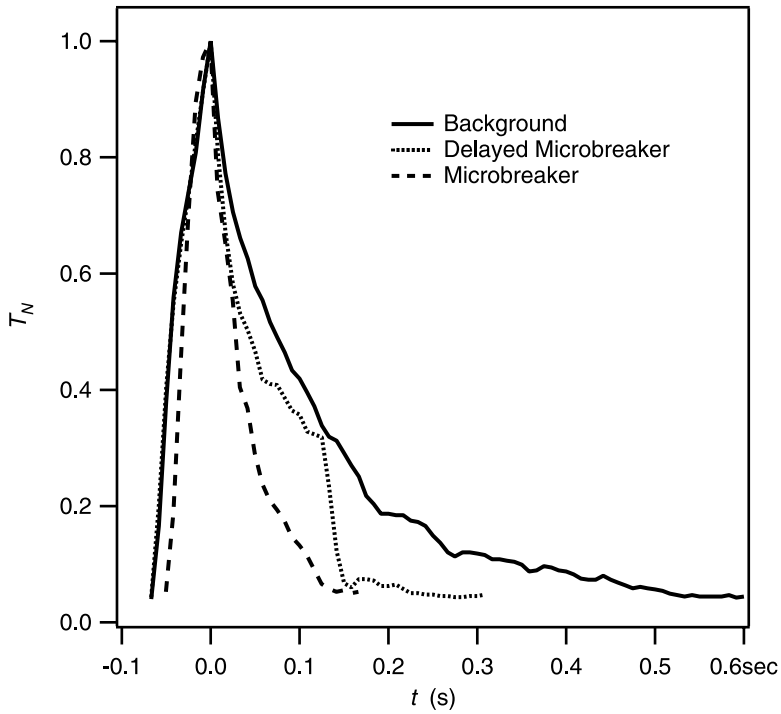

Figure 13. Time series of the ACFT patch decay. Examples include decay affected directly by microscale breaking (microbreaker), decay affected by microscale breaking after some time (delayed microbreaker), and decay not affected by microscale breaking (background).

background increases, as does wind-driven shear, and hence the surface renewal and gas transfer increase. The ratio of k_{B600} to k_{NB600} serves as an estimate of the enhancement of k_{H600} due to microscale wave breaking. The turbulence generated by the actively breaking microscale wave crest consistently enhances the local transfer velocity with a mean enhancement factor of 3.4 ± 0.6 for all experiments. Our measurements show that microscale wave breaking has a significant effect on the increased transfer velocity of heat across the air-water interface in the presence of waves. Additionally, although our data show that k_{H600} is not equivalent to k_{G600}, the data do show that both transfer velocities scale similarly for increases in turbulence and microscale breaking. Therefore it is logical that the enhancement factor due to microscale breaking observed for k_{H600} would also be observed for k_{G600}.

3.4. Comparisons of Wave Slope, Gas Transfer, and Microbreaking

[34] Figure 15 shows the correlation of k_{H600} with $\langle S^2 \rangle$ with a coefficient of determination r^2 of 0.90 for a least squares linear regression. Because this value is slightly less than the value of $r^2 = 0.94$ for the correlation of k_{H600} with A_B, it is not unexpected that comparison of Figure 11 with Figure 15 shows that A_B is a better correlate for k_{H600} than $\langle S^2 \rangle$. The appearance of the data in Figure 15 and the corresponding r^2 value are comparable to results reported by *Jähne et al.* [1984] and *Bock et al.* [1999] for k_{G600} correlated with $\langle S^2 \rangle$. For a given $\langle S^2 \rangle$, k_{H600} for cleaned cases is greater than k_{H600} for the surfactant-influenced cases, which is not the case for the correlation of k_{H600} with A_B. The hydrodynamical reasons for this difference are not clear at present, but it does suggest that scaling transfer velocities in terms of a parameter such as A_B, which is directly related to microscale wave breaking is to be preferred over scaling to an indirect parameter like $\langle S^2 \rangle$.

[35] The microscale breaking process is the culminating event in the development of capillary-gravity wave packets, and the breaking process dissipates energy into near-surface turbulence that enhances k_{H600}. Since k_{H600} correlates with A_B and microbreaking has been shown to directly enhance k_{H600}, it is possible that microbreaking may serve as a link between the observed correlation of k_{H600} with $\langle S^2 \rangle$. Figure 16 shows A_B increases with $\langle S^2 \rangle$ and, similar to Figure 15, this relationship is a function of surface cleanliness. While, for a given $\langle S^2 \rangle$, A_B may be slightly greater for cleaned cases versus surfactant-influenced cases, the relationship suggests that microbreaking may be the process that links the observed correlation of gas transfer to wave slope.

[36] The slope imagery in Figure 4 shows the very front of the curved bore-like crest to have the steepest slope, and this steep slope corresponds directly to the leading edge of the propagating thermal front of the microscale breaking signature in the infrared. The slope image also shows only extremely short capillary waves that are barely visible riding on the forward face at the initial moment of disruption. These short capillary waves were measured to be of $O(10^{-3})$ m in wavelength, corresponding to phase speeds of roughly 60 to 70 cm s^{-1} which is in the same range as the measured phase speed of the breaking steep-sloped front. The surging bore-like crest and the region behind it appear distinctly "dimpled," suggesting that an energetic process occurs right at the crest. This highly three-dimensional dimpled characteristic of the bore-like crest and of the wake diminishes in subsequent slope images, but in the infrared imagery the microscale breaker is shown to continue to

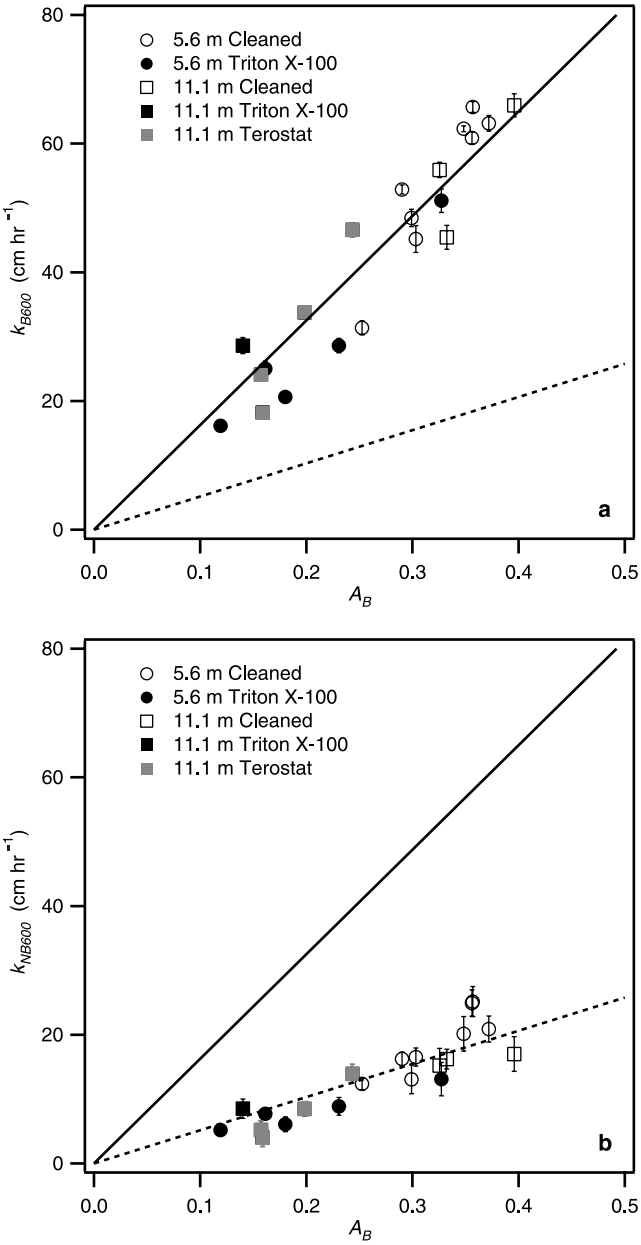

Figure 14. Local transfer velocities as determined by ACFT referenced to $Sc = 600$ for (a) decay patches affected directly by microscale breaking, k_{B600}, and (b) those in the background, k_{NB600}, as a function of A_B. Solid lines represent regression of k_{B600} against A_B (slope = 161.5 ± 4.5, $r^2 = 0.95$), and dashed lines represent k_{NB600} against A_B (slope = 51.6 ± 2.4, $r^2 = 0.89$). Both regressions are forced through origin. See Figure 5 caption for description of legend.

disrupt the surface. While the dimpled features diminish, short capillary waves begin to emerge on the forward face of the front of the bore-like crest and continue to grow in wavelength. The wavelengths of capillary waves in Figure 4 were measured to increase by at least a factor of two, corresponding to a decrease in the phase speeds to roughly 40 to 50 cm s^{-1}. This decrease is in the same range as the measured phase speeds of the dominant wave in the spectrum and of the slowed individual breaking front. An examination of 30 individual events shows that the actively breaking wave crest gains speed as it breaks and subsequently slows to the phase speed of the dominant wave. At the same time, the wavelength of the capillary waves adjusts to the phase speed of the breaking crest according to the dispersion relation.

[37] The combination of infrared and wave slope imagery has been utilized to investigate the contribution of roughness features associated with microbreaking to $\langle S^2 \rangle$, in a manner similar to that used to discriminate between ACFT patches affected and unaffected by microbreakers. Using the thresholded outline of the disruption of the thermal boundary layer by microscale breaking as a mask, the slope is calculated for the region within A_B as Breaking and for the region $(1 - A_B)$ as the background. The analysis of the data set was limited to three experiments (experiment 5, U = 6.9 m s^{-1}, cleaned surface; experiment 8, U = 5.5 m s^{-1}, cleaned surface; experiment 13, U = 6.9 m s^{-1}, Triton X-100) of simultaneous and colocated infrared and wave slope imagery at the 5.6 m fetch. These experiments span the range of k_{H600}, A_B, and $\langle S^2 \rangle$ of this study.

[38] Figure 17 shows short time series of the mean square slope within the detected microbreaker area, $\langle S^2 \rangle_B$, and the mean square slope in the background, $\langle S^2 \rangle_{NB}$. The event in the time series in Figure 17 labeled E corresponds to the image sequence shown in Figure 4. Three additional breaking events occur within the time series and are labeled A, C, and D. The event labeled B is a capillary-gravity wave packet that did not exhibit the infrared signature of breaking. The time series shows strong enhancement of slope due to microscale wave breaking signified by large spikes in $\langle S^2 \rangle_B$. As the microscale breaking Event E appears within the infrared and slope imagery in Figure 4, $\langle S^2 \rangle_B$ spikes to roughly 50% greater than $\langle S^2 \rangle_{NB}$ just as the wave begins to

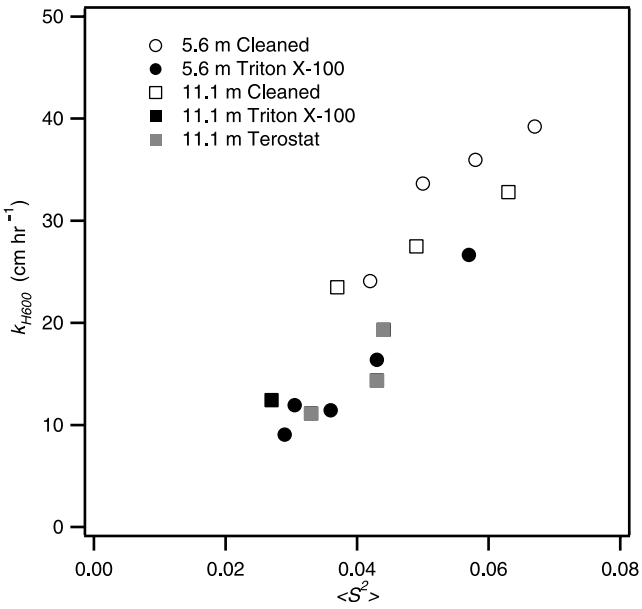

Figure 15. The local heat transfer velocity, k_{H600}, versus the total mean square slope, $\langle S^2 \rangle$. See Figure 5 caption for description of legend.

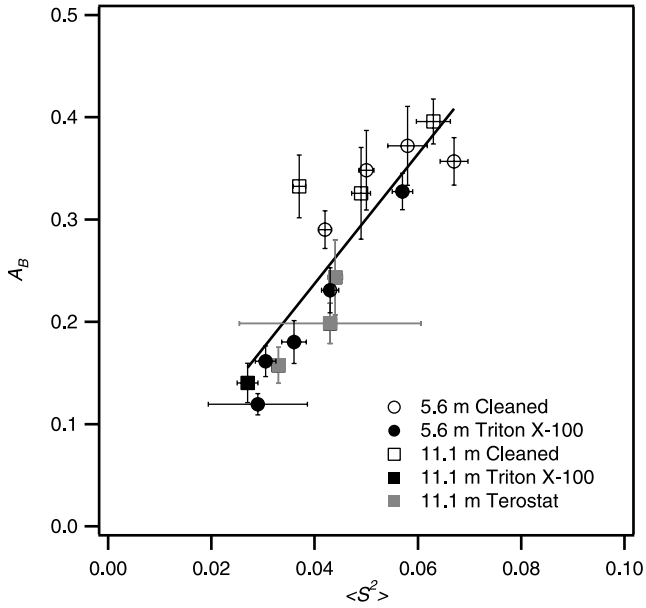

Figure 16. The fractional area coverage of microscale wave breaking, A_B, versus the total mean square slope, $\langle S^2 \rangle$. See Figure 5 caption for description of legend.

break. As the microscale breaker propagates through the image, the extent of the wake left behind by the breaking wave increases, and $\langle S^2 \rangle_B$ decreases. The concentrated, steep slopes observed in Figure 4 during the initiation of breaking contribute significantly to $\langle S^2 \rangle_B$. Subsequently, the slope decreases simultaneous with the increase in A_B. Events A, C, and D show the more characteristic increase in $\langle S^2 \rangle_B$ to double that of $\langle S^2 \rangle_{NB}$, followed by the decrease in $\langle S^2 \rangle_B$ with the increase in A_B. Note that no significant $\langle S^2 \rangle_B$ is observed during B and that, when observed, the values for $\langle S^2 \rangle_B$ are half that of $\langle S^2 \rangle_{NB}$. This example is characteristic of the wave slope enhancement due to microscale breaking. The mean enhancement of $\langle S^2 \rangle_B$ over $\langle S^2 \rangle_{NB}$ was 10% for the 3 experiments analyzed.

4. Discussion

4.1. Functional Form of the Relationship Between k_{H600} and A_B

[39] A nonlinear regression through all the data in Figure 11 would be intuitively consistent since gas transfer will continue to occur for $A_B = 0$ and gas transfer will continue to increase as A_B becomes saturated with increasing wind speed. We propose that k_{H600} should be correlated with A_B for low to moderate wind speeds based on the partitioning model in equation (10) presented in section 3.3. If k_B and k_{NB} are constant, k_H will be linearly correlated with A_B. As we have shown here, k_B and k_{NB} are not constant and k_H is therefore nonlinearly correlated with A_B.

[40] This partitioning model in equation (10) can be simplified to be purely dependent upon A_B using independent estimates for k_B and k_{NB} on the right hand side of the relationship based upon the data presented here. Given the linear relationship between k_{B600} and A_B in Figure 14 and the mean enhancement factor between k_{B600} and k_{NB600} of 3.4, the partitioning model in equation (10) becomes quadratic with respect to A_B with the particular functional form

$$k_{H600} = 114.7A_B^2 + 47.8A_B. \tag{11}$$

The relationship between k_{H600} and A_B in equation (11) is plotted as the solid line in Figure 11. When compared to the least squares linear regression of the data shown as the dashed line in Figure 11, application of equation (11) results in an improved correlation that is consistent with our expectation of a nonlinear behavior. For $A_B > 0.35$, which corresponds to wind speeds higher than 8.1 m s^{-1} for a clean water surface, the data in Figure 11 suggest that equation (11) does not adequately describe the relationship between k_{H600} and A_B at higher wind speeds. One possible explanation for this is that

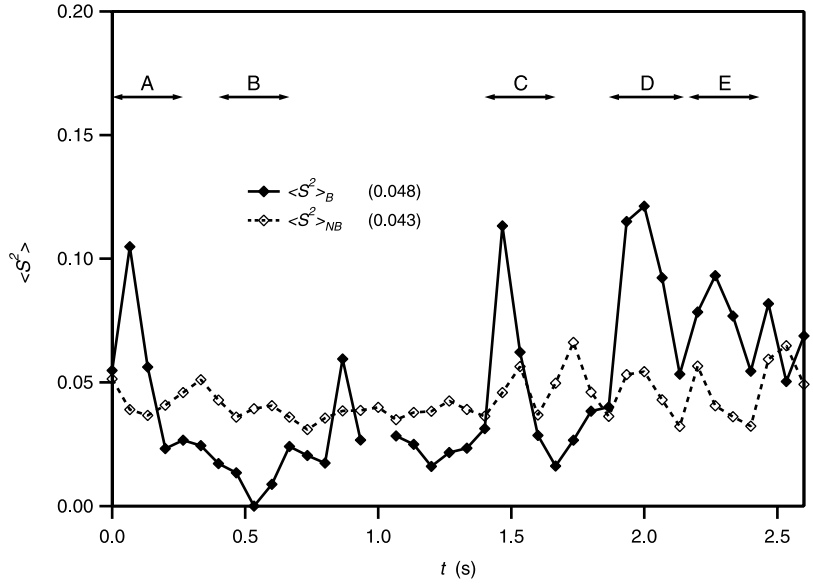

Figure 17. Time series of $\langle S^2 \rangle_B$ and $\langle S^2 \rangle_{NB}$ during experiment number 5 and including data determined from Figure 4.

for the conditions in the wind-wave tank, wind speeds of 8.1 m s^{-1} are at the onset of large-scale breaking. Once large-scale breaking is observed, it is unlikely that the relationship between k_{H600} and A_B will apply. In the limit of decreasing A_B approaching no microbreaking ($A_B < 0.1$), the data in Figure 11 suggest that gas exchange will be greater than implied by the partitioning model for $A_B = 0$. It is expected that turbulent processes not associated with microbreaking, such as those driven by buoyancy, shear, and small-scale Langmuir circulation, will contribute to k_{H600} in this limit. It is also likely that the nonlinear dependence will be a function of surfactant concentration and possibly other parameters such as atmospheric stability. In light of these observations, it is clear that the behavior of the relationship is more nonlinear than the partitioning model suggests and will require additional measurements in the regions for $A_B < 0.1$ and $A_B > 0.4$.

[41] Regardless of the specific functional form of the relationship between k_{H600} and A_B at low to moderate wind speeds, k_{H600} is a single-valued function of A_B in contrast to the multivalued behavior of k_{H600} with respect to U. As mentioned previously, the results of k_{G600} versus A_B in Figure 6 compare a tank-averaged to a local quantity. Since k_{H600} and A_B are both local measurements and we believe that microbreaking is the process that controls k_{H600}, it therefore follows that a correlation of k_{H600} with A_B will be independent of surface cleanliness. The data shown in Figure 11 support the assertion that microscale wave breaking is a critical surface process relating to air-water exchange.

4.2. Influence of Microbreaking on Schmidt Number Exponent

[42] The surface boundary condition should be determined by its dynamical effect on the near-surface velocity field and not by the surface cleanliness alone. Since the wave spectra in Figure 2 are strongly affected by the presence of surfactants [*Lucassen*, 1982; *Frew*, 1997] and near-surface turbulence has been linked with the presence of microscale breaking waves [*Siddiqui et al.*, 2001], the change in n with A_B in Figure 7 reveals a change in the interaction of turbulence with the air-water interface. Disruptions of the thermal boundary layer by microscale wave breaking observed in the infrared imply that the near-surface turbulence generated by these events was strong enough to produce surface divergence. According to continuity, the velocity fluctuations responsible for thinning the mass boundary layer are closely related to the divergence of the velocity field at a cleaned surface [*McKenna and McGillis*, 2004]. This suggests that locally the air-water interface behaves as a free surface. Thus, as A_B increases, the cumulative effect of these areas of surface divergence should cause n to approach $1/2$. Since waves were always present during these measurements, the flow regime was always rough. Therefore the transition of n from $2/3$ to $1/2$ can be seen as a transition from a rigid surface to a free surface boundary condition, rather than a smooth to a rough regime.

4.3. Microbreaking Enhancement of Gas Transfer

[43] The data shown in Figure 14 demonstrate that the transfer velocity within the wake of a microscale breaking wave is greater than that in the background, presumably because of the increased turbulence generated by the breaking process. The skin layer disruptions associated with microscale wave breaking events can be viewed as regions where the replacement of fluid, or surface renewal, within the mass boundary layer is enhanced. It is this area of enhanced surface renewal generated in the wake of a microscale breaking wave that regulates not only the transfer of heat, but also the transfer of gas across the air-water interface. The local measurements of k_{B600} and k_{NB600} from ACFT are directly estimated from the surface renewal properties of the turbulence at the air-water interface inside and outside the microbreaking patches, respectively. Therefore the partitioning expression in equation (10) suggests that if k_B is much greater than k_{NB}, k_H will correlate with A_B, and surface renewal due to the turbulence generated by microbreaking will contribute significantly to both heat and gas transfer.

[44] The results in Figure 14 indeed show that $k_{B600} \gg k_{NB600}$, and surface renewal in the wakes of microscale breaking waves was shown to enhance heat transfer by a factor of 3.4 over that in the background. *Siddiqui et al.* [2004, 2001] used particle image velocimetry to measure the timescales associated with coherent structures of enhanced vorticity beneath the crests and in the wakes of microbreaking waves. *Siddiqui et al.* [2004] then assumed these timescales defined the surface renewal timescales and showed that k_{G600} predicted using a surface renewal model and the measured timescales agreed with k_{G600} values measured using gaseous tracers. This provides further evidence for the theory that surface renewal caused by turbulence generated by the microbreaking waves is driving the enhanced air-water transfer observed in the local heat transfer velocity results.

[45] Figure 18 shows the ratio $R_{eff} = A_B k_{B600}/k_{H600}$ versus A_B, where k_{H600} is defined according to equation (10), as well as the theoretical curve for R_{eff} using the mean enhancement factor, k_{B600}/k_{NB600}, of 3.4. The ratio R_{eff} serves as an estimate of the effect of microscale wave breaking on the overall transfer velocity. At the lowest A_B ($U = 4.2$ m s^{-1}), the contribution of microscale wave breaking to gas transfer is 25%. As A_B increases to its maximum value at $U = 9.3$ m s^{-1}, the effect of microscale wave breaking on the total transfer velocity approaches nearly 75% and is significantly greater than the contribution of the background. Figure 19 shows the partitioned expression in equation (10) for k_{H600} based on k_{B600} and k_{NB600} versus the average k_{H600} measured using ACFT in section 2.2. The comparison in Figure 19 shows that equation (10) describes the average k_{H600} from ACFT very well. These results show conclusively that microscale wave breaking is an underlying mechanism that explains the observation of enhanced gas transfer in the presence of waves and governs air-water gas transfer at low to moderate wind speeds.

[46] That k_{H600} from equation (10) compares well with the overall transfer velocity from ACFT suggests that the analysis is consistent with the results and that the expression properly describes the surface renewal processes that affect gas transfer. Surface renewal due to microscale wave breaking and to shear or convectively driven turbulence in the background are both accounted for in the model. Only at low k_{H600} does equation (10) underestimate k_{H600}. At these low k_{H600} values and correspondingly low A_B values, a

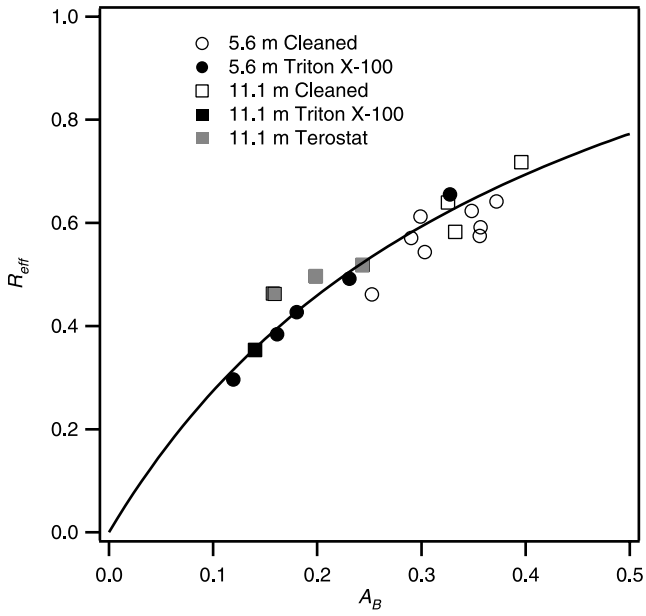

Figure 18. The ratio $R_{eff} = A_B k_{B600}/k_{H600}$ as a function of A_B, where k_{H600} is determined according to equation (10), as well as the theoretical curve for R_{eff} using the mean enhancement factor, k_{B600}/k_{NB600}, of 3.4. See Figure 5 caption for description of legend.

secondary mechanism not detected as a microscale breaking wave, such as small-scale Langmuir circulation, may begin to be of importance in determining air-water transfer velocities. Small-scale Langmuir circulation has been observed in laboratory wind-wave initiation studies by *Melville et al.* [1998] and was shown to be both persistent and energetic. *Veron and Melville* [2001] showed that the initiation of increased levels of heat transfer was related to the onset of small-scale Langmuir circulation and turbulence in the absence of microbreaking. The comparison of the partitioning expression in equation (10) to the overall k_{H600} and the results in Figure 18 demonstrate that the potential for microscale wave breaking to dominate gas transfer is of significant importance when considering the processes that affect air-sea exchanges of heat and mass.

[47] The success of the partitioning expression in equation (10) in describing k_{H600} cannot go without comment on its potential weaknesses. First, the model assumes that the measured k_{B600} is constant when applied over the region A_B. This will contribute error since k_{B600} is an average of the complete distribution of the transfer velocities detected within A_B. Some breaking events may be actively breaking while others may be decaying turbulent wakes. The intensity of the individual breaking events may vary as well. Therefore a representative distribution of all stages, scales, and strengths of breaking must be included in the average k_{B600}. The model also assumes that A_B is detected correctly as the effective area in microbreaking-induced transfer. Variability in the frequency and spatial extent of microbreaking are expected to be modulated by, among other things, fetch, atmospheric stability, and swell, and in turn may modify the estimate of the contribution due to breaking found in this study. Future laboratory and field experiments should measure a larger distribution of events than sampled here in order to estimate k_B properly and to investigate the effect of varying environmental conditions on both A_B and k_B.

4.4. Relationship of Microbreaking to Wave Slope and Gas Transfer

[48] The infrared and wave slope measurements presented in section 3.1 and 3.4 suggest a relationship between microscale wave breaking and the correlation of gas transfer with $\langle S^2 \rangle$. Substantial increases in slope due to short-crested, or three-dimensional, roughness features have been observed in the actively breaking bore-like crest of a microscale breaking wave and within its dimpled wake. These roughness features are observed in microscale breaking events that occur during both cleaned and surfactant-influenced cases, and both with and without capillary waves. Both these roughness features associated with microbreaking and the abundant capillary-gravity waves not associated with microbreaking contribute to $\langle S^2 \rangle$.

[49] We define the effective contribution to mean square slope due to breaking as $R_{SB} = A_B \langle S^2 \rangle_B / \langle S^2 \rangle_{ov}$, where $\langle S^2 \rangle_{ov}$ is the total mean square slope of the area overlapping infrared and slope images. For the subset of experiments at the 5.6 m fetch discussed in section 3.4, the average R_{SB} are shown in Figure 20 as a function of A_B and compared to the theoretical curve for R_{eff} shown in Figure 18. The results indicate that R_{SB} decreased slightly for increasing A_B, and that the contribution of microbreaking to $\langle S^2 \rangle$ is less than the contribution of microbreaking to k_{H600}. The surfactant-influenced case showed higher R_{SB} than the cleaned surface experiments, likely due to the persistence of the dimpled, small-scale disturbances within the actively breaking crest and the damping of capillary waves that otherwise would contribute to $\langle S^2 \rangle_{ov}$ for a cleaned surface. In the present approach, R_{SB} becomes significant for short duration when either $\langle S^2 \rangle_B$ or A_B is large. The occasions when $\langle S^2 \rangle_B$ was observed to be

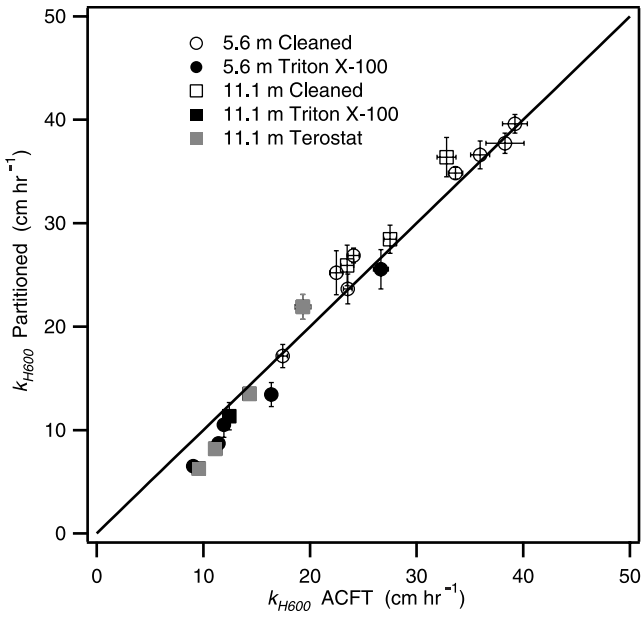

Figure 19. Comparison of k_{H600} determined from the Partitioning expression in equation (10) and k_{H600} determined from ACFT directly. See Figure 5 caption for description of legend.

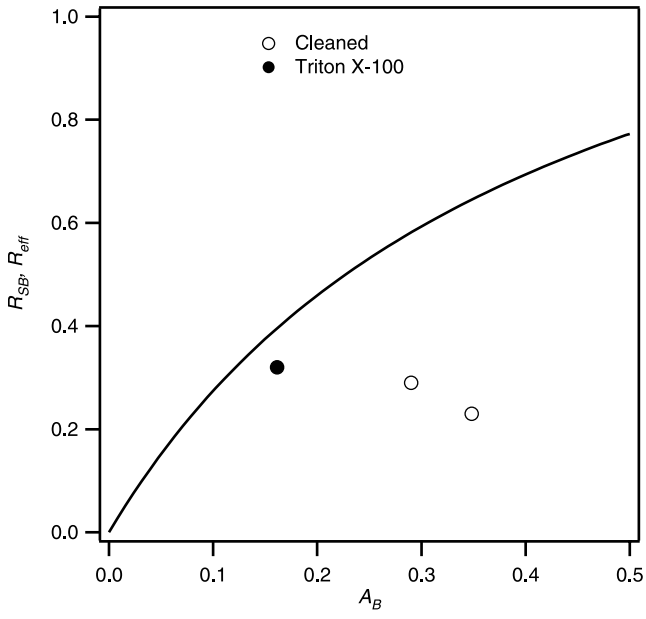

Figure 20. The ratio $R_{SB} = A_B\langle S^2\rangle_B/\langle S^2\rangle_{ov}$ (circles) at a fetch of 5.6 m as a function of A_B, as well as the theoretical curve for R_{eff} in Figure 18.

significantly greater than $\langle S^2\rangle_{NB}$, as in Figure 17, were short-lived. While microbreaking contributes to $\langle S^2\rangle$, Figure 20 suggests that the greatest contribution occurs in areas not directly affected by active microbreaking.

[50] The simultaneous infrared and wave slope imagery show that the density of capillary waves present during the microscale wave breaking process is less than for nonbreaking waves. Specifically, the capillary waves on the forward face of the bore-like crest become extremely short during the most intense initiation of microscale breaking when steep slopes occupy the bore-like crest itself. From the time that capillary waves are formed to the moment that microscale wave breaking occurs, the wave slope characteristics are constantly evolving throughout the growth process of the wave packet. The wave evolution leading up to a microbreaking incorporates contributions of slope from waves of all scale and distinction. Microscale wave breaking is merely one component of this wind-wave cycle and of short duration. Dense packets of capillary-gravity waves ubiquitous in regions not affected by microbreaking more likely will dominate the contribution to the total mean square wave slope.

[51] Since the bore-like crest produces the signature of breaking detected as A_B in the infrared imagery, only the steep slopes associated with the front of the actively breaking crest and the wake of a microscale breaker have been included in the estimate of the influence of $\langle S^2\rangle_B$ on $\langle S^2\rangle$. Capillary waves have been shown to contribute significantly to $\langle S^2\rangle$ [*Bock et al.*, 1999] and are observed to be transient during the microscale breaking process. The fact that capillary waves are damped by surfactants, coupled with the fact that the smallest-scale waves have been shown to correlate with the gas transfer velocity suggests that capillary waves characterize the importance of the wave field to gas transfer. The potential for capillary waves as a mechanism for gas transfer has been demonstrated both experimentally [*Saylor and Handler*, 1997] and theoretically [*Witting*, 1971; *Coantic*, 1986; *Szeri*, 1997]. However, we have shown that this process does not dominate. In light of our results that microbreaking controls up to 75% of the transfer, the contribution of capillary waves to k_{H600} is minimal compared to microbreaking. The contribution of capillary waves to $\langle S^2\rangle$ is symptomatic of a simultaneous increase in overall microbreaking and the densely structured capillary-gravity wave system that increases with wind forcing. The link between k_{H600} and $\langle S^2\rangle$ is more complicated than simply stating that microbreaking is the direct link according to Figure 16. It is more likely that microbreaking controls k_{H600}, the capillary-gravity wave system facilitates microbreaking, and the nonbreaking capillary and gravity waves contribute significantly to $\langle S^2\rangle$.

5. Conclusion

[52] Microscale wave breaking, through the near-surface turbulence it generates, is hypothesized to enhance heat and gas transfer. The fractional area coverage, A_B, of the surface affected by microbreaking ranged from 0.25 to 0.40 for a cleaned surface at wind speeds ranging from 4.2 to 8.3 m s^{-1}. The local heat transfer velocity was correlated with A_B and this correlation was independent of surface cleanliness and fetch. The results indeed show that $k_{B600} \gg k_{NB600}$, and surface renewal in the wakes of microbreakers was shown to enhance transfer by a factor of 3.4 over that in the background. Furthermore, microbreaking was shown to directly contribute up to 75% of the transfer across the air-water interface under moderate wind speed conditions. This is the first direct evidence that microscale wave breaking enhances the transfer velocity. The gas transfer measurements show a linear correlation of k_{H600} with k_{G600}, but k_{H600} was 2.5 times greater than k_{G600}. This suggests that microbreaking controls air-water gas transfer in a manner similar to heat transfer, but heat may not be an accurate proxy tracer for sparingly soluble gases when studying air-water exchange. Collectively, these results show conclusively that microbreaking is an underlying mechanism that explains the observation of enhanced gas transfer in the presence of waves and may govern air-sea gas transfer at low to moderate wind speeds.

[53] In the infrared imagery, the microbreaking process is observed to disrupt the aqueous thermal boundary layer, producing fine-scale surface thermal structures within the bore-like crest of the microbreaking wave and in its wake. In the slope imagery, microbreaking generates three-dimensional dimpled roughness features within the bore-like crest and in its wake. The spatial scales of the fine-scale thermal structures and the three-dimensional roughness features within the bore-like crests of microbreakers were observed to be of $O(10^{-2})$ m, same as the length scale for the vortical eddy structures measured beneath wind-forced waves by *Siddiqui et al.* [2004]. Furthermore, the dimpled roughness features of the bore-like crest correspond directly to the warmest fine-scale features of the skin layer disruption by microbreaking. The implication is that the fine-scale thermal structures and the dimpled roughness features are directly related to the near-surface turbulence generated at the bore-like crest. Because near-surface turbulence increases k_H

and k_G, microbreakers are likely to be the mechanism that enhances heat and mass transfer.

[54] The detected events of microbreaking directly enhance heat and gas transfer and produce surface roughness elements that contribute directly to $\langle S^2 \rangle$. Also, A_B was correlated with $\langle S^2 \rangle$ as shown in Figure 16. Since many capillary and nonbreaking gravity waves may dominate $\langle S^2 \rangle$, these results suggest there is an indirect link between microbreaking and the correlation of transfer velocity with $\langle S^2 \rangle$. Furthermore, the modulation of capillary waves as microscale breaking waves evolve and the transient roughness features associated with microbreaking have shown promise in identifying individual microbreaking events. A comprehensive examination of the IR and wave slope imagery data should clarify the relationship between microbreaking and $\langle S^2 \rangle$.

[55] **Acknowledgments.** The insightful comments of four reviewers helped significantly to improve this manuscript. This work was supported by National *Sc*ience Foundation grants (OCE-9633423 and OCE-9911320) to A.T.J. and W.E.A., a grant from the Space and Remote Sensing Code of the Office of Naval Research to A.T.J., the National Aeronautics and Space Administration, and the Applied Physics Laboratory at the University of Washington. This is LDEO contribution number 6643.

References

Asher, W., and R. Wanninkhof (1998), Transient tracers and air-sea gas transfer, *J. Geophys. Res.*, *103*, 15,939–15,958.

Asher, W. E., L. M. Karle, B. J. Higgins, P. J. Farley, E. C. Monahan, and I. S. Leifer (1996), The influence of bubble plumes on air-seawater gas transfer velocities, *J. Geophys. Res.*, *101*, 12,027–12,041.

Asher, W. E., A. T. Jessup, and M. Atmane (2004), Oceanic application of the active controlled flux technique for measuring air-sea transfer velocities of heat and gases, *J. Geophys. Res.*, *109*, C08S12, doi:10.1029/2003JC001862.

Atmane, M., W. E. Asher, and A. T. Jessup (2004), On the use of the active infrared technique to infer heat and gas transfer velocities at the air-water free surface, *J. Geophys. Res.*, *109*, C08S14, doi:10.1029/2003JC001805.

Banner, M. L. (1990), The influence of wave breaking on the surface pressure distribution in wind-wave interactions, *J. Fluid Mech.*, *211*, 463–495.

Banner, M. L., and O. M. Phillips (1974), On the incipient breaking of small scale waves, *J. Fluid Mech.*, *65*, 647–656.

Bock, E. J., T. Hara, N. M. Frew, and W. R. McGillis (1999), Relationship between air-sea gas transfer and short wind waves, *J. Geophys. Res.*, *104*, 25,821–25,831.

Coantic, M. (1986), A model of gas transfer across air-water interfaces with capillary waves, *J. Geophys. Res.*, *91*, 3925–3943.

Csanady, G. T. (1990), The role of breaking wavelets in air-sea gas transfer, *J. Geophys. Res.*, *95*, 749–759.

Danckwerts, P. V. (1951), Significance of liquid-film coefficients in gas absorption, *Ind. Eng. Chem.*, *43*, 1460–1467.

Downing, H. D., and D. Williams (1975), Optical constants of water in the infrared, *J. Geophys. Res.*, *80*, 1656–1661.

Frew, N. M. (1997), The role of organic films in air-sea gas exchange, in *The Sea Surface and Global Change*, edited by P. S. Liss and R. A. Duce, pp. 121–172, Cambridge Univ. Press, New York.

Harriott, P. (1962), A random eddy modification of the penetration theory, *Chem. Eng. Sci.*, *17*, 149–154.

Haußecker, H., and B. Jähne (1997), A tensor approach for precise computation of dense displacement vector fields, in *Informatik Aktuell*, edited by E. Paulus and F. M. Wahl, pp. 199–208, Springer-Verlag, New York.

Haußecker, H., S. Reinelt, and B. Jähne (1995), Heat as a proxy tracer for gas exchange measurements in the field: Principles and technical realization, in *Air-Water Gas Transfer*, edited by B. Jähne and E. C. Monahan, pp. 405–413, AEON, Hanau, Germany.

Hill, R. H. (1972), Laboratory measurement of heat transfer and thermal structure near an air-water interface, *J. Phys. Oceanogr.*, *2*, 190–198.

Jähne, B., and H. Haußecker (1998), Air-water gas exchange, *Annu. Rev. Fluid Mech.*, *14*, 321–350.

Jähne, B., W. Huber, A. Dutzi, T. Wais, and J. Ilmberger (1984), Wind/wave-tunnel experiment on the Schmidt number—and wave field dependence of air/water gas exchange, in *Gas Transfer at Water Surfaces*, edited by W. Brutsaert and G. H. Jirka, pp. 303–309, D. Reidel, Norwell, Mass.

Jähne, B., K. O. Munnich, R. Bosinger, A. Dutzi, W. Huber, and P. Libner (1987), On the parameters influencing air-water gas exchange, *J. Geophys. Res.*, *92*, 1937–1949.

Jähne, B., P. Libner, R. Fischer, T. Billen, and E. J. Plate (1989), Investigating the transfer processes across the free aqueous viscous boundary layer by the controlled flux method, *Tellus Ser. B*, *41*, 177–195.

Jähne, B., J. Klinke, and S. Waas (1994), Imaging of short ocean wind waves: A critical theoretical review, *J. Opt. Soc. Am. A Opt. Image Sci.*, *11*, 2197–2209.

Jessup, A. T., C. J. Zappa, and H. Yeh (1997), Defining and quantifying microscale wave breaking with infrared imagery, *J. Geophys. Res.*, *102*, 23,145–23,154.

Keller, W. C., and B. L. Gotwols (1983), Two-dimensional optical measurement of wave slope, *Appl. Opt.*, *22*, 3476–3478.

Klinke, J. (1996), Optical measurements of small-scale wind-generated water surface waves in the laboratory and the field, Ph.D. diss., Univ. of Heidelberg, Heidelberg, Germany.

Klinke, J., and B. Jähne (1995), Measurements of short wind waves during the MBL ARI West Coast Experiment, in *Air-Water Gas Transfer*, edited by B. Jähne and C. Monahan, pp. 165–173, AEON, Hanau, Germany.

Ledwell, J. J. (1984), The variation of the gas transfer coefficient with molecular diffusivity, in *Gas Transfer at Water Surfaces*, edited by W. Brutsaert and G. H. Jirka, pp. 293–302, D. Reidel, Norwell, Mass.

Liss, P. S., and P. G. Slater (1974), Flux of gases across the air-sea interface, *Nature*, *247*, 181–184.

Longuet-Higgins, M. S., and R. P. Cleaver (1994), Crest instabilities of gravity waves, part 1. The almost-highest wave, *J. Fluid Mech.*, *258*, 115–129.

Lucassen, J. (1982), Effect of surface-active material on the damping of gravity waves: A reappraisal, *J. Colloid Interface Sci.*, *85*, 52–58.

McAlister, E. D., and W. McLeish (1969), Heat transfer in the top millimeter of the ocean, *J. Geophys. Res.*, *74*, 3408–3414.

McAlister, E. D., and W. McLeish (1970), A radiometric system for airborne measurement of the total heat flow from the sea, *Appl. Opt.*, *9*, 2697–2705.

McKenna, S. P., and W. R. McGillis (2004), The role of free-surface turbulence and surfactants in air-water gas transfer, *Int. J. Heat Mass Transfer*, *47*, 539–553.

Melville, W. K., R. Shear, and F. Veron (1998), Laboratory measurements of the generation and evolution of Langmuir circulations, *J. Fluid Mech.*, *364*, 31–58.

Richardson, C. L. (2000), The dependence of the controlled flux technique on ambient heat flux for air-water gas transfer, M. Sci. thesis, Univ. of Wash., Seattle.

Saylor, J. R., and R. A. Handler (1997), Gas transport across an air/water interface populated with capillary waves, *Phys. Fluids*, *9*, 2529–2541.

Siddiqui, M., M. R. Loewen, C. Richardson, W. E. Asher, and A. T. Jessup (2001), Simultaneous particle image velocimetry and infrared imagery of microscale breaking waves, *Phys. Fluids*, *13*, 1891–1903.

Siddiqui, M., M. R. Loewen, W. E. Asher, and A. T. Jessup (2004), Coherent structures beneath wind waves and their influence on air-water gas transfer, *J. Geophys. Res.*, *109*, C03024, doi:10.1029/2002JC001559.

Szeri, A. J. (1997), Capillary waves and air-sea gas transfer, *J. Fluid Mech.*, *332*, 341–358.

Veron, F., and W. K. Melville (2001), Experiments on the stability and transition of wind-driven water surfaces, *J. Fluid Mech.*, *446*, 25–65.

Wanninkhof, R., and W. R. McGillis (1999), A cubic relationship between air-sea CO_2 exchange and wind speed, *Geophys. Res. Lett.*, *26*, 1889–1892.

Witting, J. (1971), Effects of plane progressive irrotational waves on thermal boundary layers, *J. Fluid Mech.*, *50*, 321–334.

Wu, J. (1971), An estimation of oceanic thermal-sublayer thickness, *J. Phys. Oceanogr.*, *1*, 284–286.

Zappa, C. J. (1999), Microscale wave breaking and its effect on air-water gas transfer using infrared imagery, Ph.D. dissertation, Univ. of Wash., Seattle.

Zappa, C. J., A. T. Jessup, and H. H. Yeh (1998), Skin-layer recovery of free-surface wakes: Relationship to surface renewal and dependence on heat flux and background turbulence, *J. Geophys. Res.*, *103*, 21,711–21,722.

Zappa, C. J., W. E. Asher, and A. T. Jessup (2001), Microscale wave breaking and air-water gas transfer, *J. Geophys. Res.*, *106*, 9385–9391.

W. E. Asher and A. T. Jessup, Applied Physics Laboratory, University of Washington, 1013 NE 40th Street, Seattle, WA 98105, USA. (asher@apl.washington.edu; jessup@apl.washington.edu)

J. Klinke, Physical Oceanography Research Division, Scripps Institution of Oceanography, La Jolla, CA 92093-0230, USA. (jklinke@ucsd.edu)

S. R. Long, NASA GSFC/Wallops Flight Facility, Code 972, Bldg. N-159, Rm. W-134, Wallops Island, VA 23337, USA. (steve@airsea.wff.nasa.gov)

C. J. Zappa, Lamont-Doherty Earth Observatory of Columbia University, 61 Route 9W, Palisades, NY 10964, USA. (zappa@ldeo.columbia.edu)